

Extragalactic magnetism with SOFIA (SALSA Legacy Program) - V: First results on the magnetic field orientation of galaxies*

ALEJANDRO S. BORLAFF,^{1,2} ENRIQUE LOPEZ-RODRIGUEZ,² RAINER BECK,³ SUSAN E. CLARK,^{4,2} EVANGELIA NTORMOUSI,^{5,6}
KONSTANTINOS TASSIS,^{7,6} SERGIO MARTIN-ALVAREZ,² MEHRNOOSH TAHANI,² DANIEL A. DALE,⁸
IGNACIO DEL MORAL-CASTRO,^{9,10} JULIA ROMAN-DUVAL,¹¹ PAMELA M. MARCUM,¹ JOHN E. BECKMAN,^{12,10} AND
KANDASWAMY SUBRAMANIAN^{13,14}

¹NASA Ames Research Center, Moffett Field, CA 94035, USA

²Kavli Institute for Particle Astrophysics & Cosmology (KIPAC), Stanford University, Stanford, CA 94305, USA

³Max-Planck-Institut für Radioastronomie, Auf dem Hügel 69, 53121 Bonn, Germany

⁴Department of Physics, Stanford University, Stanford, California 94305, USA

⁵Scuola Normale Superiore di Pisa, Piazza dei Cavalieri 7, Pisa, Italy

⁶Institute of Astrophysics, Foundation for Research and Technology-Hellas, Vasilika Vouton, GR-70013 Heraklion, Greece

⁷Department of Physics & ITCP, University of Crete, GR-70013, Heraklion, Greece

⁸Department of Physics and Astronomy, University of Wyoming, Laramie, WY 82071, USA

⁹Kapteyn Astronomical Institute, University of Groningen, PO Box 800, 9700 AV Groningen, The Netherlands

¹⁰Facultad de Física, Universidad de La Laguna, Avda. Astrofísico Fco. Sánchez s/n, 38200, La Laguna, Tenerife, Spain

¹¹Space Telescope Science Institute, 3700 San Martin Drive, Baltimore, MD 21218

¹²Instituto de Astrofísica de Canarias, C/ Vía Láctea, E-38200 La Laguna, Tenerife, Spain

¹³IUCAA, Post Bag 4, Ganeshkhind, Pune 411007, India

¹⁴Department of Physics, Ashoka University, Rajiv Gandhi Education City, Rai, Sonapat 131029, Haryana, India

ABSTRACT

We present the analysis of the magnetic field (B -field) structure of galaxies measured with far-infrared (FIR) and radio (3 and 6 cm) polarimetric observations. We use the first data release of the Survey on extragalactic magnetism with SOFIA (SALSA) of 14 nearby (< 20 Mpc) galaxies with resolved ($5'' - 18''$; 90 pc–1 kpc) imaging polarimetric observations using HAWC+/SOFIA from 53 to 214 μm . We compute the magnetic pitch angle (Ψ_B) profiles as a function of the galactocentric radius. We introduce a new magnetic alignment parameter (ζ) to estimate the disordered-to-ordered B -field ratio in spiral B -fields. We find FIR and radio wavelengths to not generally trace the same B -field morphology in galaxies. The Ψ_B profiles tend to be more ordered with galactocentric radius in radio ($\zeta_{6\text{cm}} = 0.93 \pm 0.03$) than in FIR ($\zeta_{154\mu\text{m}} = 0.84 \pm 0.14$). For spiral galaxies, FIR B -fields are 2–75% more turbulent than the radio B -fields. For starburst galaxies, we find that FIR polarization is a better tracer of the B -fields along the galactic outflows than radio polarization. Our results suggest that the B -fields associated with dense, dusty, turbulent star-forming regions, those traced at FIR, are less ordered than warmer, less-dense regions, those traced at radio, of the interstellar medium. The FIR B -fields seem to be more sensitive to the activity of the star-forming regions and the morphology of the molecular clouds within a vertical height of few hundred pc in the disk of spiral galaxies than the radio B -fields.

1. INTRODUCTION

Polarimetric observations allow the tracing of magnetic fields (B -field) in galaxies. Synchrotron emission is expected to emerge largely from the warm and diffuse ISM, due to a combination of a large volume fraction for the ubiquitous cosmic ray electron population and thermal gas emission.

While this emission is considerably sensitive to Faraday rotation, it should be relatively less affected by depolarization from disordered B -field structures due to larger coherence scales for the field and a prevalence of the mean magnetic field (Evirgen et al. 2017). The FIR polarization arises from thermal emission of magnetically aligned dust grains tracing a weighted density medium along the line-of-sight (LOS) and within the beam of a dense ($\log_{10}(N_{\text{HI}+\text{H}_2} [\text{cm}^{-2}]) = [20, 23]$) and cold ($T_{\text{d}} = [20, 50]$ K) component of the ISM in galaxies (Lopez-Rodriguez et al. 2022a, SALSA IV). The differences between radio and FIR polarimetric observations allow us to investigate extragalactic B -fields in different ISM phases, something that is uniquely enabled by the Survey

Corresponding author: Alejandro S. Borlaff

a.s.borlaff@nasa.gov

* The SOFIA Legacy Program for Magnetic Fields in Galaxies provides a software repository at <https://github.com/galmagfields/hawc>, and publicly available data at <http://galmagfields.com/>

for extragalactic magnetism with SOFIA (SALSA) Legacy Program (Lopez-Rodriguez et al. 2022a, SALSA IV).

In fact, while radio polarization and FIR observations trace the same large-scale ordered B -field¹ structure in the less-dense interarm regions, significant divergence has been found in the spiral arms of M51 (Borlaff et al. 2021, SALSA I). This result may be due to the different thermodynamical properties between the warm diffuse ISM and the cold dust filaments associated with star forming regions and molecular clouds. In the closest merger of two spiral galaxies, the Antennae galaxies, the FIR B -field closely follows the relic spiral arm, while the radio B -field is mostly radial (Lopez-Rodriguez et al. 2022b, SALSA VI). This result suggests that the FIR B -field may be cospatial with the molecular gas in the midplane of the relic spiral arm, while the radio B -field seems to be more aligned with the dynamics of the HI gas on an extraplanar layer above the disk affected by the merger activity. In addition, the 1 kpc-scale starburst ring of NGC 1097 has a compressed and constant FIR B -field at the intersection with the galactic bar, while the radio B -field has a spiral morphology tightly cospatial with the diffuse neutral gas (Lopez-Rodriguez et al. 2021c, SALSA II). To observe the B -field within the cold and dense ISM affected by the star formation activity and molecular clouds, FIR polarimetric observations are necessary.

In this paper, we explore the structure of the B -field in a quantitative approach probed by the FIR and radio for a sample of 14 galaxies with diverse morphologies (grand-design spirals, post-merger, starbursts). The associated FIR polarimetry data (Section 2.1) are from the SALSA Legacy Program (PI: Lopez-Rodriguez, E. & Mao, S. A.), obtained with the High-Angular Wideband Camera Plus (HAWC+; Vaillancourt et al. 2007; Dowell et al. 2010; Harper et al. 2018) on board the 2.7-m Stratospheric Observatory For Infrared Astronomy (SOFIA). SOFIA/HAWC+ has an optimal combination of spatial resolution, field of view, and sensitivity for observational tests of the theoretical connections between B -field, turbulence, and star formation. FIR observations—practically impossible using ground-based observatories due to atmospheric absorption—allow us to efficiently detect the thermal emission of magnetically aligned dust grains. In addition, we will compare the results with the B -field structure measured using radio polarimetric observations for cases in which ancillary data are available (see Sec. 2.2). Sec. 3 is dedicated to the analysis of the B -field orientation maps. In Sec. 4 we quantitatively analyze the structure of the B -field pitch angle for spiral galaxies in the sample. Finally, Sec. 5 introduces a new structural parameter, ζ , dedicated to quan-

Table 1. HAWC+ configuration. *Columns, from left to right:* (a) Band name. (b) Central wavelength of the band in μm . (c) FWHM bandwidth in μm . (d) Pixel scale of the band in $''$. (e) FWHM in $''$. (f) FOV for polarimetric observations in $'$.

Band	λ_c	$\Delta\lambda$	Pixel scale	Beam size	Polarimetry FOV
	(μm)	(μm)	($''$)	($''$)	($'$)
(a)	(b)	(c)	(d)	(e)	(f)
A	53	8.7	2.55	4.85	1.4×1.7
C	89	17	4.02	7.8	2.1×2.7
D	154	34	6.90	13.6	3.7×4.6
E	214	44	9.37	18.2	4.2×6.2

tify the ordering ratio of the spiral B -field. The discussion and conclusions are presented in Secs. 6 and 7 respectively.

2. DATA

2.1. Far-infrared polarimetric observations

We analyze the B -field orientations of the galaxies using the same FIR polarimetric observations as presented in SALSA III and IV (Lopez-Rodriguez et al. 2022c,a). In summary, the FIR polarimetric observations were performed using four bands, 53, 89, 154, and 214 μm , with HAWC+ (Vaillancourt et al. 2007; Dowell et al. 2010; Harper et al. 2018) onboard the 2.7-m SOFIA telescope. Table 1 shows the HAWC+ configuration for every band. The observations were performed using the on-the-fly-mapping (OTFMAP) polarimetric mode described in SALSA III (Lopez-Rodriguez et al. 2022c). The exception is M51: this galaxy was observed using the chopping and nodding technique and reduced as described by Borlaff et al. (2021). Table 2 shows the galaxy sample and the associated bands. The pixel scale of the final data product is equal to the detector pixel scale (i.e. Nyquist sampling) in any given band (Table 1). For a detailed description of the analysis of the polarization fraction, see SALSA IV. Table 3 shows the properties of the galaxy sample.

2.2. Radio polarimetric observations

Ancillary radio polarimetric observations at 3 and 6 cm are used for the analysis. Table 2 shows the radio polarimetric data that were publicly available and kindly shared by the authors of the associated manuscripts. These datasets were obtained using observations of the Effelsberg 100-m single-dish radio-telescope, in combination with datasets from the Karl G. Jansky Very Large Array (VLA) when available. We refer to the original manuscripts shown in Table 2 for a complete description of the observations and analysis of the datasets used in our work. Longer wavelength (18, 20 cm) observa-

¹ *Ordered fields* are defined to be what polarized FIR emission or synchrotron emission at short radio wavelengths (where Faraday depolarization is small) measures within the telescope beam, projected to the plane perpendicular to the line of sight. Contributions for ordered fields come from *anisotropic random fields*, whose average over the beam vanishes, and *regular fields*, whose average over the beam is finite. To distinguish between these contributions, additional Faraday rotation data in the radio range are needed.

tions can be strongly affected by Faraday rotation (Beck et al. 2019), and are thus not considered in this work.

For each galaxy and radio wavelength, the Stokes IQU were convolved with a Gaussian kernel to match the beam size (full-width-half-maximum; FWHM) of HAWC+ at the bands shown in Table 2. Then, we reprojected each radio polarimetric observation to the associated HAWC+ observations per galaxy and per band to match the same pixel scale and field-of-view (FOV). Finally, the fractional and angle of polarization, and polarized flux were computed, accounting for the level of polarization bias. To avoid biased results due to the number of measurements across the galaxy, we only use radio polarization measurements that are spatially coincident with the HAWC+ observations. The radio polarization maps are used to spatially correlate the polarization arising from synchrotron emission with that arising from thermal emission by means of magnetically aligned dust grains observed with HAWC+. Throughout this manuscript, the results at 3 and 6 cm are very similar, within their uncertainties.

3. MAGNETIC FIELD ORIENTATION MAPS

3.1. Methodology

Figures 1 – 6 show the B -field orientation maps of the galaxies associated with the first data release of SALSA (SALSA IV, Lopez-Rodriguez et al. 2022a) at FIR wavelengths and radio wavelengths (when available, see Table 2). The FIR polarization measurements with at least $PI/\sigma_{PI} \geq 2.0$ and $P \leq 20\%$ were selected for all galaxies, with customized I/σ_I to avoid contamination from the background, as shown in the Appendix (Table 6), where σ_{PI} and σ_I are the uncertainties per pixel of the polarized flux density and Stokes I , respectively. We have rotated the measured polarization angles by 90° to show the inferred B -field orientations in the plane of the sky. For radio polarization measurements, all pixels with $PI/\sigma_{PI} \leq 2.0$ and $I/\sigma_I \leq 2$ were excluded, as well as those pixels that contain no significant FIR polarization emission. As mentioned in Section 2.2, radio polarimetric observations were smoothed and reprojected to the HAWC+ observations. For visualization purposes, all figures in this manuscript have a constant polarization length to show the B -field orientation.

Measuring the average B -field orientation allows us to quantify the effects of the different spatial resolutions in the observations. We provide two different estimations of the average B -field position angle: $\langle PA_B^{\text{hist}} \rangle$ and $\langle PA_B^{\text{int}} \rangle$. $\langle PA_B^{\text{hist}} \rangle$ is defined as the average of the B -field position angles of the individual polarization measurements after quality cuts. $\langle PA_B^{\text{hist}} \rangle$ is estimated using the circular mean as

$$\langle PA_B^{\text{hist}} \rangle = \text{atan2} \left(\sum_{i=1}^N \sin PA_{B,i}, \sum_{i=1}^N \cos PA_{B,i} \right) \quad (1)$$

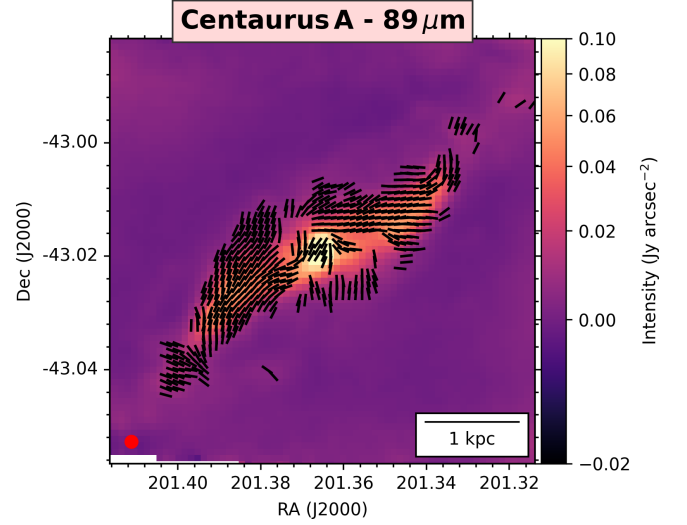


Figure 1. FIR B -field orientation maps of Centaurus A. Surface brightness (colorscale) represents total intensity in FIR ($89 \mu\text{m}$). Polarization measurements have been set to have a constant length to show the inferred B -field orientation (black dashes). Polarization measurements with $PI/\sigma_{PI} \geq 2.5$, $P \leq 20\%$, and $I/\sigma_I \geq 10$ were selected.

where $PA_{B,i}$ is the B -field orientations of N individual polarization measurements.

$\langle PA_B^{\text{int}} \rangle$ is the integrated B -field orientation of the galaxy disk, estimated as

$$\langle PA_B^{\text{int}} \rangle = \frac{1}{2} \arctan \left(\frac{\langle U \rangle}{\langle Q \rangle} \right) + \frac{\pi}{2} \quad (2)$$

where $\langle U \rangle$ and $\langle Q \rangle$ are the average of the Stokes QU for pixels with $I/\sigma_I \geq 20$ in the FIR observations.

The difference between $\langle PA_B^{\text{hist}} \rangle$ and $\langle PA_B^{\text{int}} \rangle$ is that the latter is the average orientation of the B -field in the case of unresolved observations (assigning higher weights to pixels with larger PI). In addition, $\langle PA_B^{\text{int}} \rangle$ is measure of the degree of non-axisymmetry of the field pattern, e.g. zero for a perfectly spiral pattern in a mildly inclined galaxy, but large for a field aligned with the disk of a strongly inclined galaxy. The uncertainty is a measurement of the accuracy of the polarization angle of an unresolved galaxy. In contrast, $\langle PA_B^{\text{hist}} \rangle$ is an estimation of the circular average B -field orientation on all the analyzed independent beams across the galaxy disk, not weighted by PI , allowing to contrast with $\langle PA_B^{\text{int}} \rangle$ how the average position angle of the polarization maps is modified with sufficient spatial resolution. The uncertainty is a measurement of the angular dispersion of the distribution of B -field orientations within the galaxy disk.

Figure 7 shows the histograms of the B -field orientations in bins of 10° for all the individual polarization measurements per galaxy and per band at FIR (filled histograms) and 6 cm (black solid lines) wavelengths. We show the estimations of $\langle PA_B^{\text{hist}} \rangle$ per galaxy and per band. The 1σ un-

Table 2. FIR and radio polarimetric data. *Columns, from left to right:* (a) Galaxy name. (b) Central wavelength of the HAWC+ bands. (c) Physical scale of the beam at each HAWC+ band, (d) Central wavelength of the band at radio wavelengths. (e) References of the radio polarimetric observations.

Galaxy	FIR	$\theta_{\text{beam,pc}}$	Radio	References
(a)	(μm)	(pc)	(cm)	(e)
Centaurus A	89	128	-	-
Circinus	53, 89, 214	98, 157, 367	-	-
M51	154	560	3, 6	Fletcher et al. (2011)
M82	53, 89, 154, 214	90, 144, 251, 337	3, 6	Adebahr et al. (2013, 2017)
M83	154	304	6	Frick et al. (2016a)
NGC 253	89, 154	131, 229	3, 6	Heesen et al. (2011)
NGC 1068	53, 89	335, 539	-	-
NGC 1097	89, 154	719, 1254	3, 6	Beck et al. (2005)
NGC 2146	53, 89, 154, 214	400, 644, 1123, 1504	-	-
NGC 3627	154	333	3, 6	Soida et al. (2001)
NGC 4736	154	346	3, 6	Chyży & Buta (2008)
NGC 4826	89	210	-	-
NGC 6946	154	444	6	Beck (1991, 2007)
NGC 7331	154	1025	-	-

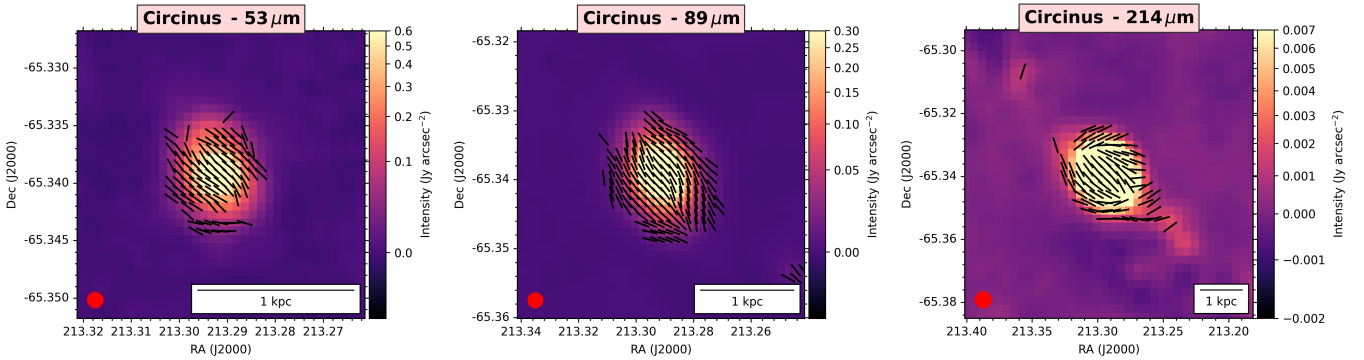


Figure 2. FIR B -field orientation maps of Circinus (53, 89, and 214 μm , from left to right). Surface brightness (colorscale) represents total intensity in each band. Polarization measurements have been set to have a constant length to show the inferred B -field orientation (black lines). We refer to Table 6 for the quality cuts in PI/σ_{PI} , P , and I/σ_I for each band.

certainty is estimated as the standard deviation of the histogram. As mentioned in Section 2.2, we only use radio polarization measurements that are spatially coincident with the HAWC+ observations. The comparison between $\langle PA_B^{\text{hist}} \rangle$ and $\langle PA_B^{\text{int}} \rangle$ for the FIR and radio observations are shown in Figure 8. The tabulated data can be found in Appendix A (Table 6).

3.2. Results

We present the results from the analysis of the morphology of the B -field estimated using FIR and radio observations. We divide our sample into starburst and/or high inclination galaxies (without a clear spiral pattern, Sec. 3.2.1) and low inclination spiral galaxies (with a spiral B -field pattern, Sec. 3.2.2).

3.2.1. Starbursts and/or high inclination galaxies

Centaurus A (Fig. 1) shows a B -field orientation tightly following the 3 kpc warped molecular disk as previously

Table 3. Galaxy Sample. *Columns, from left to right:* (a) Galaxy classification and name. \odot : face-on spiral galaxies with a spiral B -field pattern, \ast : starburst and/or edge-on galaxies without a clear spiral pattern. (b) Galaxy distance in Mpc. (c) Physical scale in pc per arcsec. (d) Galaxy type. (e) Inclination of the galaxy in degrees (face-on $i = 0^\circ$, edge-on $i = 90^\circ$). (f) Position angle of the large axis of the galaxy in the plane of the sky. (g) References associated to the distance, inclination and tilt angles.

Galaxy	Distance ¹ (Mpc)	Scale (pc'')	Type [*] ($^\circ$)	Inclination (i) ² ($^\circ$)	Tilt (θ) ² ($^\circ$)	References
(a)	(b)	(c)	(d)	(e)	(f)	(g)
\ast Centaurus A	3.42	16.42	S0pec/Sy2/RG	$83 \pm 6^\dagger$	114 ± 4	¹ Ferrarese et al. (2007); ² Quillen et al. (2010)
\ast Circinus	4.20	20.17	SA(s)b/Sy2	40 ± 10	205 ± 10	¹ Tully et al. (2009); ² Jones et al. (1999)
\odot M51	8.58	41.21	Sa	22.5 ± 5	-7 ± 3	¹ McQuinn et al. (2017); ² Colombo et al. (2014)
\ast M82	3.85	18.49	I0/Sbrst	$76 \pm 1^\dagger$	64 ± 1	¹ Vacca et al. (2015); ² Mayya et al. (2005)
\odot M83	4.66	22.38	SAB(s)c	25 ± 5	226 ± 5	¹ Tully et al. (2013); ² Crosthwaite et al. (2002)
\ast NGC 253	3.50	16.81	SAB(s)c/Sbrst	$78.3 \pm 1.0^\dagger$	52 ± 1	¹ Radburn-Smith et al. (2011); ² Lucero et al. (2015)
\odot NGC 1068	14.40	69.16	(R)SA(rs)b/Sy2	40 ± 3	286 ± 5	¹ Bland-Hawthorn et al. (1997); ^b Brinks et al. (1997)
\odot NGC 1097	19.10	92.21	SB(s)b/Sy1	41.7 ± 0.6	133.0 ± 0.1	¹ Willick et al. (1997); ² Hsieh et al. (2011)
\ast NGC 2146	17.20	82.61	SB(s)ab/Sbrst	63 ± 2	140 ± 2	¹ Tully (1988); ² Tarchi et al. (2004)
\odot NGC 3627	8.90	42.75	SAB(s)b	52 ± 1	176 ± 1	¹ Kennicutt et al. (2003); ² Kuno et al. (2007)
\odot NGC 4736	5.3	25.46	SA(r)ab	36 ± 7	292 ± 2	¹ Kennicutt et al. (2003); ² Dicaire et al. (2008)
\odot NGC 4826	5.60	26.89	(R)SA(rs)ab	65 ± 5	125 ± 5	¹ Kennicutt et al. (2003); ² Braun et al. (1994)
\odot NGC 6946	6.80	32.66	Sc	38.4 ± 3.0	239 ± 1	¹ Karachentsev et al. (2000); ² Daigle et al. (2006)
\odot NGC 7331	15.7	75.40	SA(s)b	78.1 ± 2.7	165 ± 1.2	¹ Kennicutt et al. (2003); ² Daigle et al. (2006)

^{*}Galaxy type from NASA/IPAC Extragalactic Database (NED; <https://ned.ipac.caltech.edu/>)

reported by Lopez-Rodriguez (2021a). The $\langle PA_B^{\text{hist}} \rangle$ and $\langle PA_B^{\text{int}} \rangle$ are measured to be $121 \pm 28^\circ$ and $126 \pm 9^\circ$, respectively. The large angular dispersion of $\pm 28^\circ$ was attributed to turbulence at spatial scales smaller than the beam of the observations driven by the merger activity and star-forming regions across the warped molecular disk.

We measure an almost constant B -field orientation within the central 1 kpc of the Circinus galaxy (Fig. 2). Note that the B -field orientation bends around the core at all wavelengths, which may indicate that the measured B -field is arising from the central starburst ring (Elmouttie et al. 1998b; Zschaechner et al. 2016). The $\langle PA_B^{\text{hist}} \rangle$ changes from 53° at $53 \mu\text{m}$ to 32° at $89 \mu\text{m}$, with a similar, within the uncertainties, $\langle PA_B^{\text{int}} \rangle$. At $214 \mu\text{m}$, the $\langle PA_B^{\text{int}} \rangle$ is dominated by the highly polarized regions in the bar of the galaxy with a large-scale B -field at $179 \pm 2^\circ$. The B -field orientation in the central 1 kpc at $214 \mu\text{m}$ is consistent with the B -field at 53 and $89 \mu\text{m}$. Radio polarimetric observations at 6 cm with a beam size of $9''$ show two radio lobes cospatial with the ionization cones and a spiral B -field at scales of $1'$ north and south of the unpolarized core (Elmouttie et al. 1998a).

NGC 1097 shows a constant FIR B -field orientation within the central 1 kpc starburst ring as previously reported by Lopez-Rodriguez et al. (2021c, SALSA II). Here, we present a new analysis of the $154 \mu\text{m}$ B -field orientation measure-

ments. The $\langle PA_B^{\text{int}} \rangle$ and $\langle PA_B^{\text{hist}} \rangle$ are measured to be $\sim 127^\circ$ and $\sim 132^\circ$ with associated uncertainties of $\sim 32^\circ$ and $\sim 16^\circ$, respectively (Table 6). The $154 \mu\text{m}$ B -field is parallel to the galaxy bar (which goes from South-East to North-West in the image). The radio polarimetric observations show a spiral B -field pattern within the central 1 kpc of the starburst ring of NGC 1097 (Beck et al. 2005).

M82's B -field orientation at FIR and radio polarization maps show large morphological differences (Fig. 3). The $53 - 214 \mu\text{m}$ show a B -field orientation perpendicular to the disk indicating the presence of a galactic outflow with a diameter of 1 kpc at the center of the galaxy extending $\sim 2 - 3$ kpc above and below the galaxy's disk. The B -field orientation is parallel to the disk of the galaxy from a radius of 1 to 3 kpc. The M82 results are compatible with the previous 53 and $154 \mu\text{m}$ observations reported by Jones et al. (2019); Lopez-Rodriguez et al. (2021a). Here, we present deeper observations covering a wider wavelength range, i.e. $53 - 214 \mu\text{m}$, and larger extension (> 1 kpc). At 3 and 6 cm, the B -field orientation in M82 is mainly parallel to the galactic disk (Adebahr et al. 2017). Depolarization due to Faraday rotation or the lifetime of cosmic ray electrons along the galactic outflows may cause unpolarized regions (Section 6.3). Interestingly, the radio B -field to the north and south of

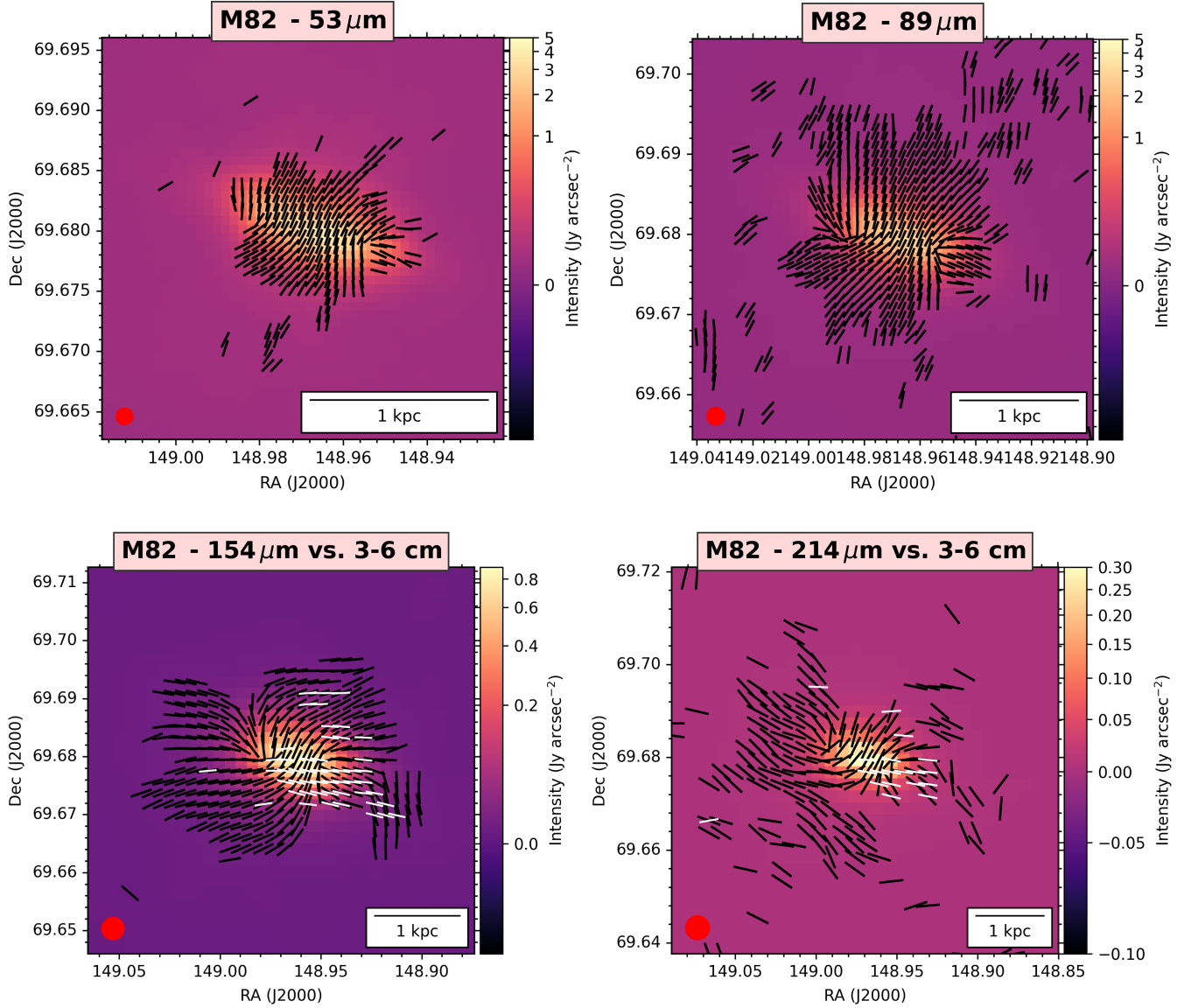


Figure 3. FIR B -field orientation maps of M82 (53, 89, 154, and 214 μm , from left to right, top to bottom). The maps in 154 μm and 214 μm show the radio polarimetric observations from Adebahr et al. (2013, 2017) in 3 and 6 cm (averaged). Surface brightness (colorscale) represents total intensity in each band. Polarization measurements have been set to have a constant length to show the inferred B -field orientation (black lines), while the radio polarization observations are represented with white lines. We refer to Table 6 for the quality cuts in PI/σ_{PI} , P , and I/σ_I for each band.

the galaxy disk is coincident with the B -field orientation at 154 μm (Fig. 3).

For NGC 253 (Fig. 4), the B -field orientation is predominantly parallel to the disk of the galaxy at both 89 and 154 μm . A B -field parallel to the disk of the galaxy at 89 μm was also measured using HAWC+ by Jones et al. (2019). At 89 μm , both $\langle PA_B^{\text{hist}} \rangle$ and $\langle PA_B^{\text{int}} \rangle$ are in agreement, within the uncertainties, with a B -field parallel to the disk. However, a change of $\Delta PA_B = |\langle PA_B^{\text{int}} \rangle - \langle PA_B^{\text{hist}} \rangle| = 103 \pm 61^\circ$ is detected at 154 μm . Our hypothesis is that this angular change is mainly due to the highly polarized, $\sim 3 - 5\%$, regions with a B -field twisting within the central 1 kpc of the

galaxy with an hourglass shape. This twisted shape may be the signature of the galactic outflow associated with its central starburst. This B -field structure has also been observed at radio wavelengths (Heesen et al. 2011). Deeper observations are required to statistically detect this trend at FIR wavelengths. Note that our released 89 and 154 μm observations only account for the 33% and 18% of the total requested time (SALSA III and IV), but these data are deeper and complementary observations to those presented by Jones et al. (2019).

For the starburst galaxy NGC 2146 (Fig. 5), the B -field orientation is parallel to the galactic outflow within the 53 – 154

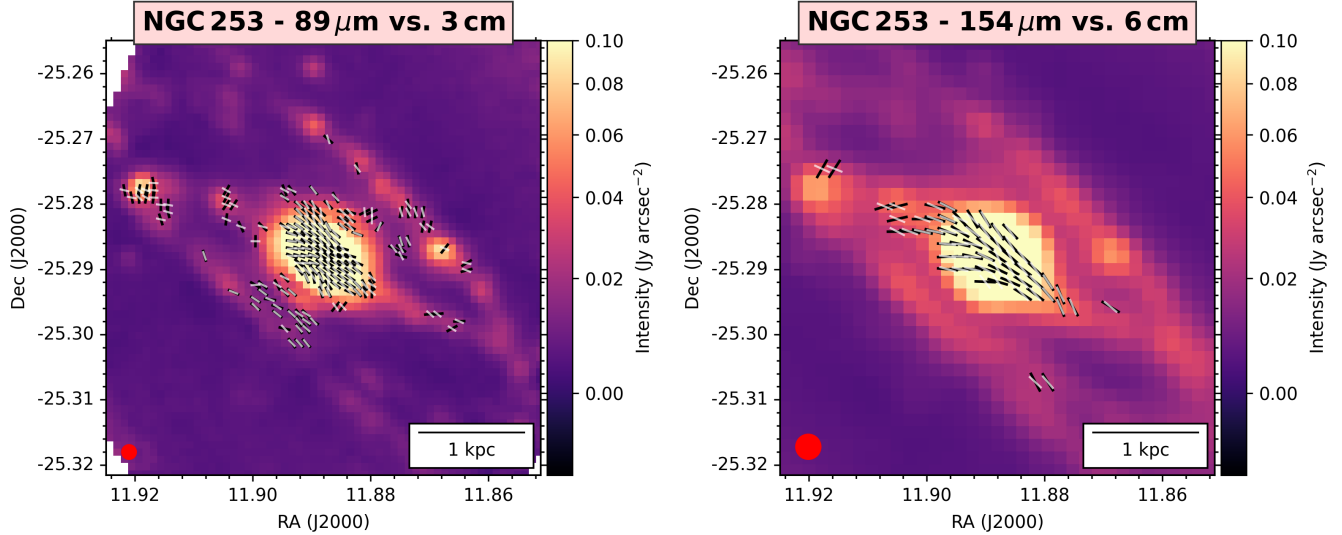


Figure 4. FIR and radio B -field orientation maps of NGC 253 ($89 \mu\text{m}$ vs. 3 cm and $154 \mu\text{m}$ vs. 6 cm , from left to right). The FIR B -field is represented with black lines, while the radio polarization observations (Heesen et al. 2011) are represented with white lines. The surface brightness (colorscale) represents total intensity in each band. The polarization vectors have been set to a constant length to show the inferred B -field orientation. We refer to Table 6 for the quality cuts in PI/σ_{PI} , P , and I/σ_I for each band.

μm wavelength range. At 53 and $89 \mu\text{m}$, the B -field orientation is aligned with the galactic outflow with a diameter of 2 kpc at the center of the galaxy. At $214 \mu\text{m}$, the B -field orientation is dominated by a component parallel to the disk of the galaxy. The B -field orientation at $154 \mu\text{m}$ is more complex showing the transition between a B -field dominated by the galactic outflow at $53 - 89 \mu\text{m}$ to a B -field dominated by the galactic disk at $214 \mu\text{m}$.

For both M82 and NGC 2146, the histograms show a change in $\langle PA_B^{\text{hist}} \rangle$ and $\langle PA_B^{\text{int}} \rangle$ from 53 to $214 \mu\text{m}$ (Figure 8 and Table 6). Specifically, $\langle PA_B^{\text{hist}} \rangle$ and $\langle PA_B^{\text{int}} \rangle$ changes from $\sim 150^\circ$ and $\sim 64^\circ$ (parallel to the outflows) to $\sim 55^\circ$ and $\sim 120^\circ$ (parallel to the disk) in M82 and NGC 2146, respectively. These results show that the resolved and unresolved FIR polarimetric observations are sensitive to the B -fields in the warm, $\sim 30 - 50\text{K}$ at $50 - 100 \mu\text{m}$, dust of galactic outflows and cold, $\sim 10 - 30\text{K}$ at $100 - 220 \mu\text{m}$, dust in the galactic disk.

In summary:

- The edge-on galaxy Centaurus A has a highly inclined B -field mostly parallel to the 3 kpc warped disk of the galaxy. The large-scale B -field shows large angular dispersion across the galactic disk driven by the merger and star-forming activity (Lopez-Rodriguez et al. 2021a).
- The B -field orientation in Circinus is mostly constant and parallel to the inner-bar and the starburst ring in the central 1 kpc .
- The starburst galaxies M82, NGC 253, and NGC 2146 show signatures of a B -field orientation potentially associated parallel to galactic outflows up to $\sim 3 \text{ kpc}$

scales above and below the disk. For M82, the B -field is parallel to the galactic outflow at all wavelengths (Jones et al. 2019; Lopez-Rodriguez 2021a). The median orientation of the FIR B -field of NGC 2146 changes with wavelength from parallel ($53 - 89 \mu\text{m}$) to perpendicular ($154 - 214 \mu\text{m}$) with respect to the galactic outflow driven by the central starburst. For NGC 253, the B -field is mostly parallel to the galaxy disk with a signature of an hour-glass shape driven by the starburst activity in the central 1 kpc .

- For M82, the radio B -field orientation is parallel to the galaxy disk, although some hint of the galactic outflow is also measured and coincident with the $154 \mu\text{m}$ B -field.

3.2.2. Spiral galaxies

The FIR B -field orientation maps of the spiral galaxies are shown in Fig. 6. The histograms of B -field orientations for the polarization measurements are presented in Fig. 7. For all the low-inclination galaxies, the $\langle PA_B^{\text{hist}} \rangle$ at FIR and radio wavelengths are mostly flat as expected from a spiral pattern.

All galaxies show a large-scale spiral B -field, except for NGC 6946. NGC 6946 shows a highly disordered FIR B -field spatially located within the star-forming regions in the spiral arms. The radio polarimetric observations show a well-ordered spiral B -field pattern, although it is aligned with the interarm regions ('magnetic arms'), instead of the morphological spiral arms. However, we detect signs of a spiral pattern in radio and FIR also in the morphological spiral arms (see Sec. 4).

Another remarkable result is the well-ordered 1 kpc -scale spiral B -field over the starburst ring of NGC 4736 at both

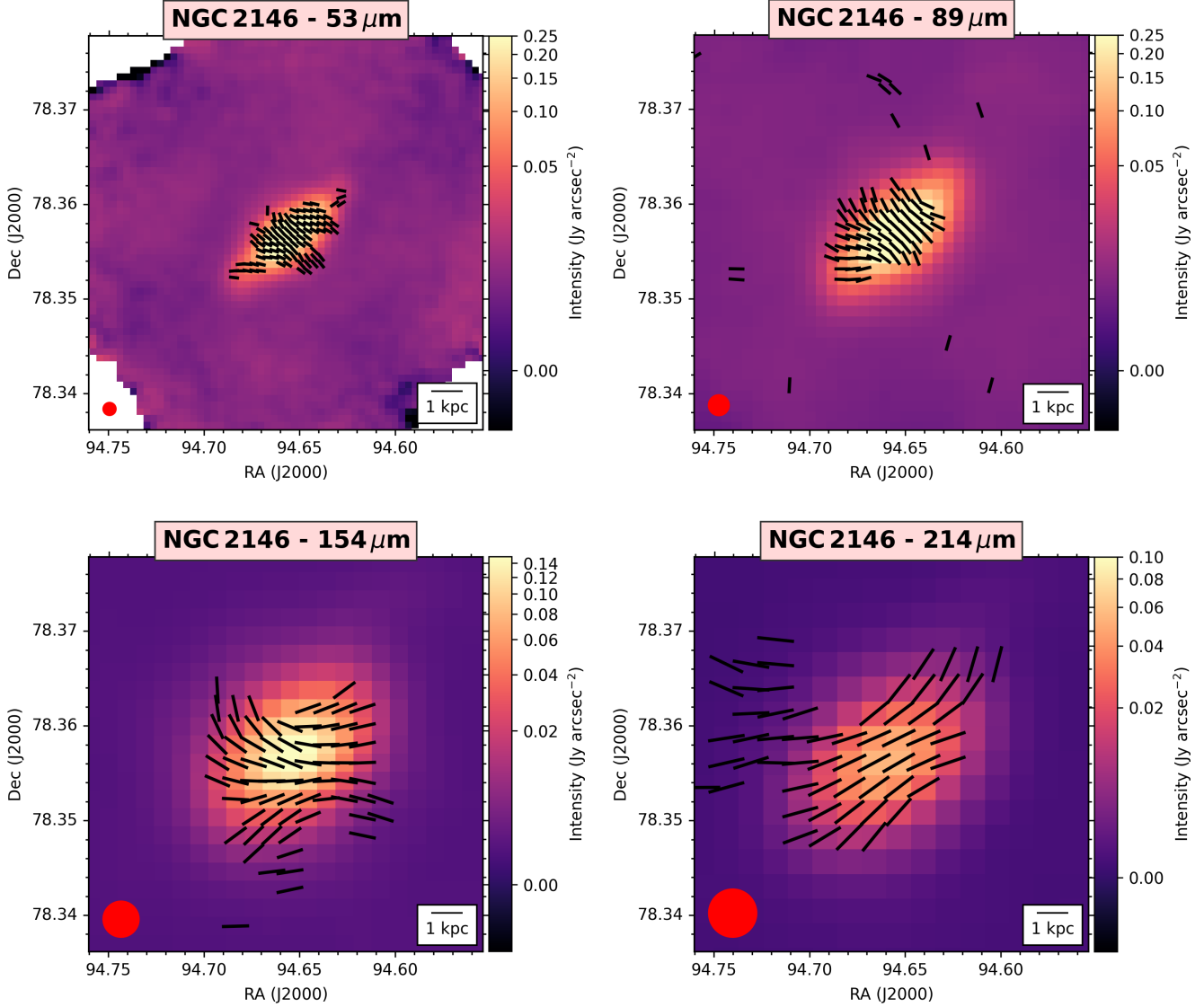


Figure 5. FIR and radio B -field orientation maps of NGC 2146 ($53 \mu\text{m}$, $89 \mu\text{m}$, $154 \mu\text{m}$, $214 \mu\text{m}$, from left to right). FIR B -field is represented with black lines. Surface brightness (colorscale) represents total intensity in each band. Polarization measurements have been set to have a constant length to show the inferred B -field orientation. Measurements with $PI/\sigma_{PI} \geq 3.0$, $P \leq 20\%$, and $I/\sigma_I \geq 20$ were selected.

FIR and radio wavelengths (Fig. 6). For both tracers, the measured spiral B -field seems to be uncorrelated with the underlying morphological structure. We measure a similar $\langle PA_B^{\text{hist}} \rangle$ of $85 \pm 42^\circ$ and $81 \pm 45^\circ$ at $154 \mu\text{m}$ and 6 cm, respectively. We note that the southern region of the galaxy has slightly different B -field orientations at radio wavelengths, while in the northern region both FIR and radio wavelengths have similar B -field orientations. Sections 4 and 5 present a quantification of these differences.

NGC 3627 presents a well-ordered spiral B -field that follows the inner morphological spiral pattern at $154 \mu\text{m}$, 3 cm, and 6 cm. Interestingly, beyond $90''$ from the galactic center, the FIR magnetic orientation deviates from the morphological arms (see North-East region), as opposed to the observed structure in 3 and 6 cm. In Sec. 4 we will analyze in detail

how this change in orientation translates into a break in the magnetic pitch angle profile very similar to the results obtained in M 51 (Borlaff et al. 2021).

We detect a spiral B -field morphology in both NGC 4826 and NGC 7331. For each galaxy, the $\langle PA_B^{\text{hist}} \rangle$ and $\langle PA_B^{\text{int}} \rangle$ are in agreement, within their uncertainties (Table 6), which indicates that the B -field is aligned with the major axis of the galaxy. This result is due to the high inclination $> 65^\circ$ of these galaxies. NGC 4826 presents a non-regular spiral B -field, with the majority of the polarization measurements located in the southern half of the galaxy. Interestingly, only the southern section was found to be polarized also in 18 and 22 cm by Heald et al. (2009), a potential consequence of Faraday depolarization. Section 4 shows the associated radial profiles of the magnetic pitch angles of these galaxies. Ra-

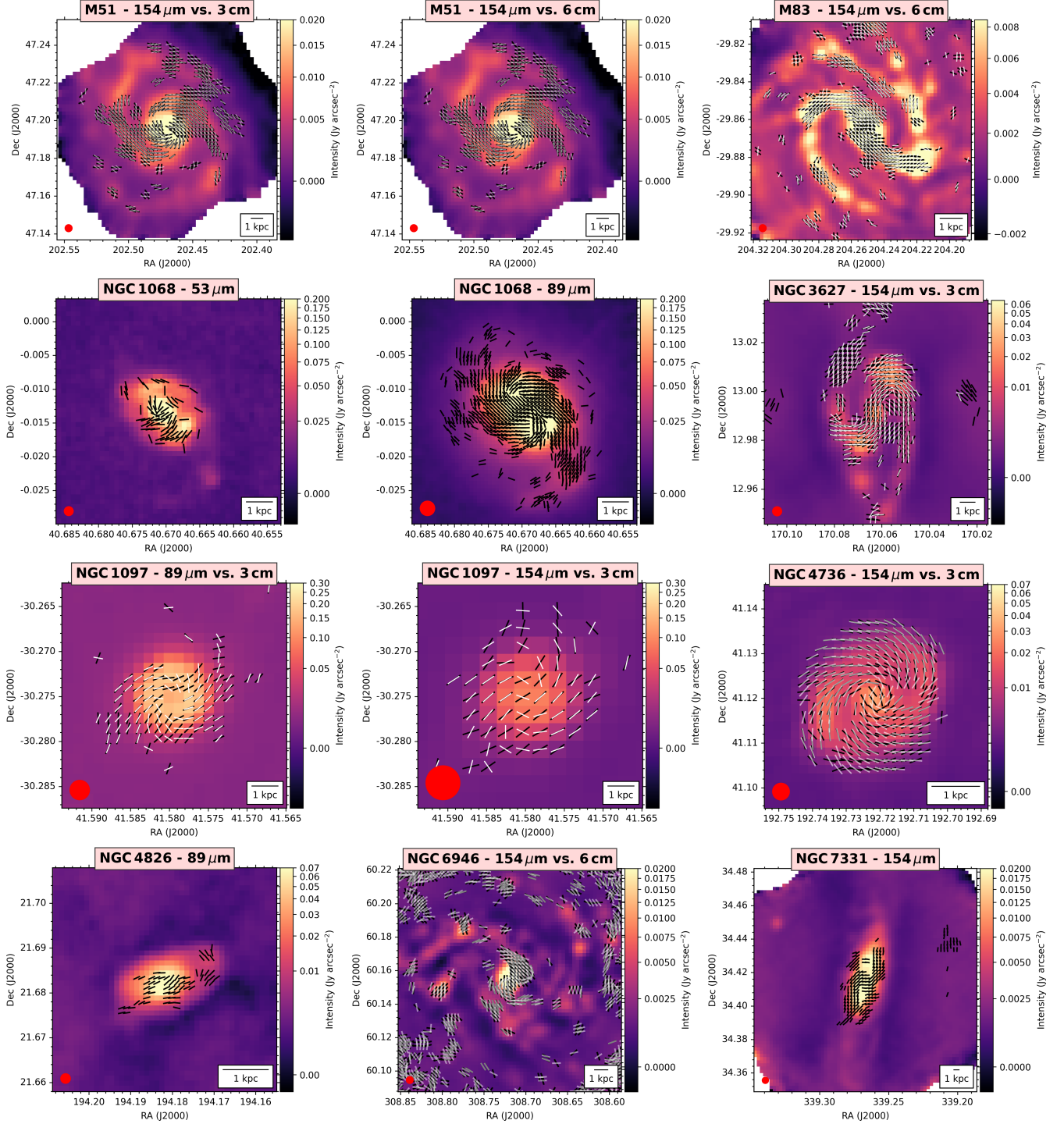


Figure 6. FIR and radio B -field orientation maps of the spiral galaxies. From left to right, top to bottom: M 51, M 83, NGC 1068, NGC 3627, NGC 1097, NGC 4736, NGC 4826, NGC 6946, and NGC 7331 (wavelengths indicated in the titles). FIR B -field (53, 89, 154, and 214 μm) is represented with black lines, while radio polarization observations (3, 6 cm) are represented with white lines, if available (see Table 2). Surface brightness (colorscale) represents total intensity in each band. Polarization measurements have been set to have a constant length to show the inferred B -field orientation. Measurements with $PI/\sigma_{PI} \geq 2.0$, $P \leq 20\%$, and $I/\sigma_I \geq 20$ were selected.

radio polarimetric observations covering the several kpc-scale of the host galaxy of NGC 7331 are unavailable.

For M 51 and M 83, the overall B -field morphology is the same in both FIR and radio polarimetric observations.

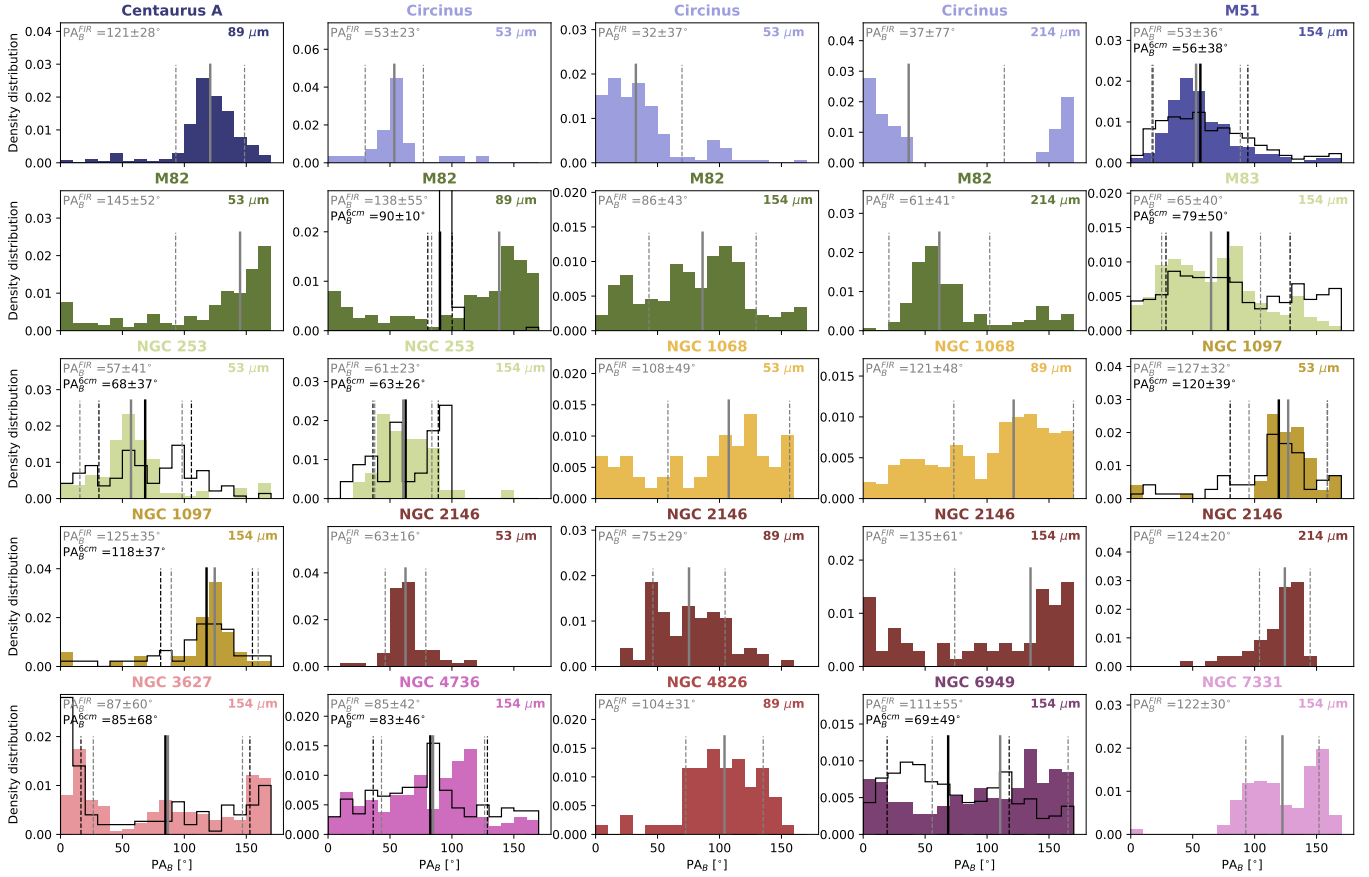


Figure 7. Histograms of the B -field orientations. The histograms are set to 10° bins, each galaxy is shown in a unique color, and the mean (grey solid line, Eq. 1) and 1σ uncertainty (grey dashed line) for the FIR observations are shown. For the galaxies with radio polarimetric observations, the histograms of the B -field orientations at 6 cm (black step histogram) with the mean (black solid line, Eq. 1) and 1σ uncertainty (black dashed line) are shown.

The B -field orientation map of M51 is the same as presented by Borlaff et al. (2021), where the pitch angles of the spiral arms at the outskirts of M51 are different at FIR and radio wavelengths. Section 4 shows the associated radial profiles of the magnetic pitch angles of these galaxies.

NGC 6946 shows a highly disordered FIR B -field orientation spatially located with the star-forming regions in the spiral arms. Fig. 6 shows the B -field pattern traced by both FIR and radio polarimetric observations, revealing clear large structural differences. At radio wavelengths, a large-scale well-ordered spiral B -field has been measured (Beck 1991, 2007). At FIR wavelengths, we detect a spiral B -field in the central ~ 3 kpc diameter. At larger galactocentric radius ($R > 3$ kpc), the B -field orientation is highly disordered in the spiral arms. The histogram of B -field orientations (Fig. 7) shows an almost flat distribution with a $\langle PA_B^{\text{hist,FIR}} \rangle = 111 \pm 55^\circ$ at $154 \mu\text{m}$ and $\langle PA_B^{\text{hist,Radio}} \rangle = 69 \pm 49^\circ$ at 6 cm.

The B -field orientation in NGC 1068 is compatible with the previous $89 \mu\text{m}$ observations reported by Lopez-Rodriguez et al. (2020a). Here, we present deeper $89 \mu\text{m}$ polarimetric observations and new $53 \mu\text{m}$ polarimetric obser-

ations. We detect a 6 kpc-scale spiral B -field at $89 \mu\text{m}$, in comparison with the 3 kpc scale detected by Lopez-Rodriguez et al. (2020a). The new $53 \mu\text{m}$ polarimetric observations show a change of $\sim 90^\circ$ at the core of NGC 1068 with respect to the $89 \mu\text{m}$. This angular offset may be due to a transition from dichroic absorption to dichroic emission or that the $53 \mu\text{m}$ is resolving the beginning of the spiral arm within the central 1 kpc.

In summary:

- The spiral galaxies M51, M83, NGC 1068, NGC 3627, and NGC 4736 present large-scale spiral ordered B -fields.
- NGC 4736 has a FIR and radio spiral B -field without clear spatial correspondence with the underlying morphology in total emission.
- NGC 6946 does not present well-ordered large-scale spiral FIR B -fields, in comparison with the well-ordered large-scale spiral B -field at radio wavelengths. The FIR B -field seems to be dominated by turbulence, potentially connected to star formation activity.

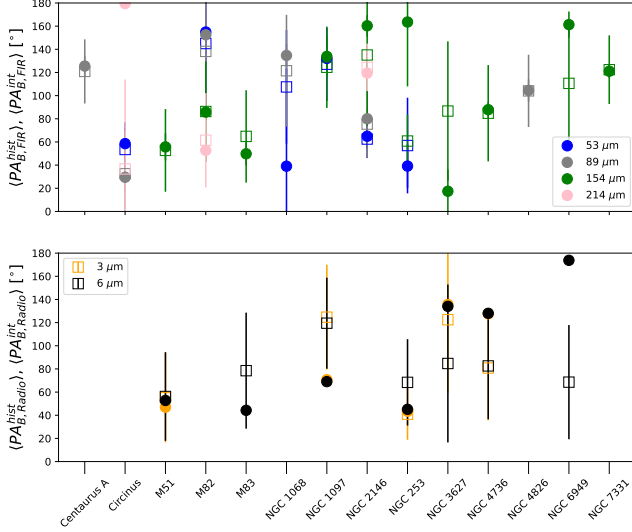


Figure 8. Mean and integrated B -field orientation of galaxies. B -field orientation at FIR (top) and radio (bottom) from individual measurements, $\langle PA_B^{\text{hist}} \rangle$ (open square, Eq. 1), and from the integrated Stokes QU , $\langle PA_B^{\text{int}} \rangle$ (filled circle, Eq. 2) are shown. Tabulated values are shown in Table 6.

- Significant large-scale differences between FIR and radio polarization observations are found in several regions of M51, NGC 1097, and NGC 3627.
- For all these galaxies, deviations from the large-scale spiral B -fields are found in star-forming regions and at the edges of the nuclear bar.

4. MAGNETIC PITCH ANGLES

The methodology to estimate the magnetic pitch angle maps for FIR and radio polarization observations (Mohawc) is described in Appendix A and previously presented by Borlaff et al. (2021). This method was implemented in PYTHON and is available on the project website².

We compute the magnetic pitch angles of 8 spiral galaxies M51, M83, NGC 1068, NGC 3627, NGC 4736, NGC 4826, NGC 6946, and NGC 7331. The other galaxies have a) vertical B -fields along the galactic outflows (i.e. M82, NGC 253, and NGC 2146); b) parallel B -fields along the galactic disk in edge-on galaxies (i.e. Centaurus A); and c) constant B -fields in the central 1 kpc (i.e. Circinus, NGC 1097). For these galaxies, we do not perform any analysis based on the magnetic pitch angles with exception of the global B -field orientation histograms and integrated B -field orientation in the full disk of galaxies as described in Section 3. Thus, this section only describes the analysis of the magnetic pitch angles of spiral galaxies.

Figure 9 shows the magnetic pitch angles as a function of the galactocentric radius at FIR, Ψ_B^{FIR} , of the sample of spiral

galaxies. Our FIR observations trace the B -fields from 0.1 kpc to 5 kpc in radius for most galaxies, and up to 15 kpc in NGC 7331. We also compute the magnetic pitch angles at 3 and 6 cm, Ψ_B^{radio} , whenever available, using the same LOS measurements as those at FIR wavelengths. Table 4 shows the median magnetic pitch angles across the full galaxy disk.

The main result is that FIR and radio wavelengths do not generally trace the same B -field morphology in spiral galaxies. As reported in Borlaff et al. (2021), M51’s spiral magnetic field presents a similar structure in both radio and FIR within the central 5 kpc, showing a significant difference in the outskirts of the disk. At radii > 5 kpc, a tightening of the FIR spiral magnetic field is observed ($\overline{\Psi}_B$ in FIR changes from approximately 25° to 0° and negative values). This abrupt variation of the FIR magnetic pitch angle has been recently confirmed by independent analyses, using alternative pitch angle estimation methods (Surgent et al. 2023). This reduction of the FIR pitch angle is not observed in radio, which displays a pitch angle that opens up with galactocentric radius. Similar discrepancies between FIR and radio B -field structure are observed in the outskirts of M83. M83’s FIR polarization structure is more loosely wounded than at radio wavelengths (average $\overline{\Psi}_B = -39.8_{-2.5}^{+1.4^\circ}$ at $154 \mu\text{m}$ and $\overline{\Psi}_B = -31.2_{-2.4}^{+5.1^\circ}$ at 6 cm), and there is a trend towards more negative values in FIR not detected in radio. This behavior is opposite to what it is observed in NGC 3627 ($\overline{\Psi}_B = -38.2_{-1.3}^{+1.2^\circ}$ at $154 \mu\text{m}$ and $\overline{\Psi}_B = -47.71_{-0.01}^{+0.13^\circ}$ at 6 cm), and in the outskirts of M51 ($r > 5$ kpc).

NGC 4736 has a similar spiral B -field orientation in both FIR and radio wavelengths ($\overline{\Psi}_B = -25.33_{-0.66}^{+1.51^\circ}$ at $154 \mu\text{m}$ and $\overline{\Psi}_B = -35.0_{-2.3}^{+4.2^\circ}$ at 3 cm) within the central 2 kpc. As shown in Figure 6, the northern spiral arm of NGC 4736 has similar pitch angles in both FIR and radio wavelengths. However, the southern arm has a more tightly wounded magnetic pitch angle at FIR than at radio wavelengths.

The lack of a well-ordered spiral magnetic structure in NGC 6946 at FIR wavelengths is clear in the magnetic pitch angle profile. NGC 6946 has a regular B -field at radio wavelengths ($\Psi_{6 \text{ cm}} = -17.6_{-4.1}^{+1.7^\circ}$) and mostly random at FIR wavelengths, although signs of a certain spiral structure can be detected with high variability ($\Psi_{\text{FIR}} = -6.5_{-12.5}^{+5.0^\circ}$). The B -field morphology at FIR wavelengths is very patchy and mostly coincident with star-forming regions across the disk (SALSA IV, Lopez-Rodriguez et al. 2022a). This result is in contrast to the regular spiral B -field (‘magnetic arms’) observed at radio wavelengths (Beck 1991, 2007). The difference between the radio polarization pattern and the FIR observations is clearly visible in Fig. 6.

For those galaxies without radio polarimetric observations, we found that a) the highly inclined galaxies NGC 4826 ($\overline{\Psi}_B = -5_{-11}^{+12^\circ}$ at $89 \mu\text{m}$) and NGC 7331 ($\overline{\Psi}_B = -66.0_{-2.8}^{+1.9^\circ}$ at $154 \mu\text{m}$) have an ordered spiral B -field morphology at FIR wavelengths, and b) the spiral galaxy NGC

² Mohawc: <https://github.com/Borlaff/MOHAWC>

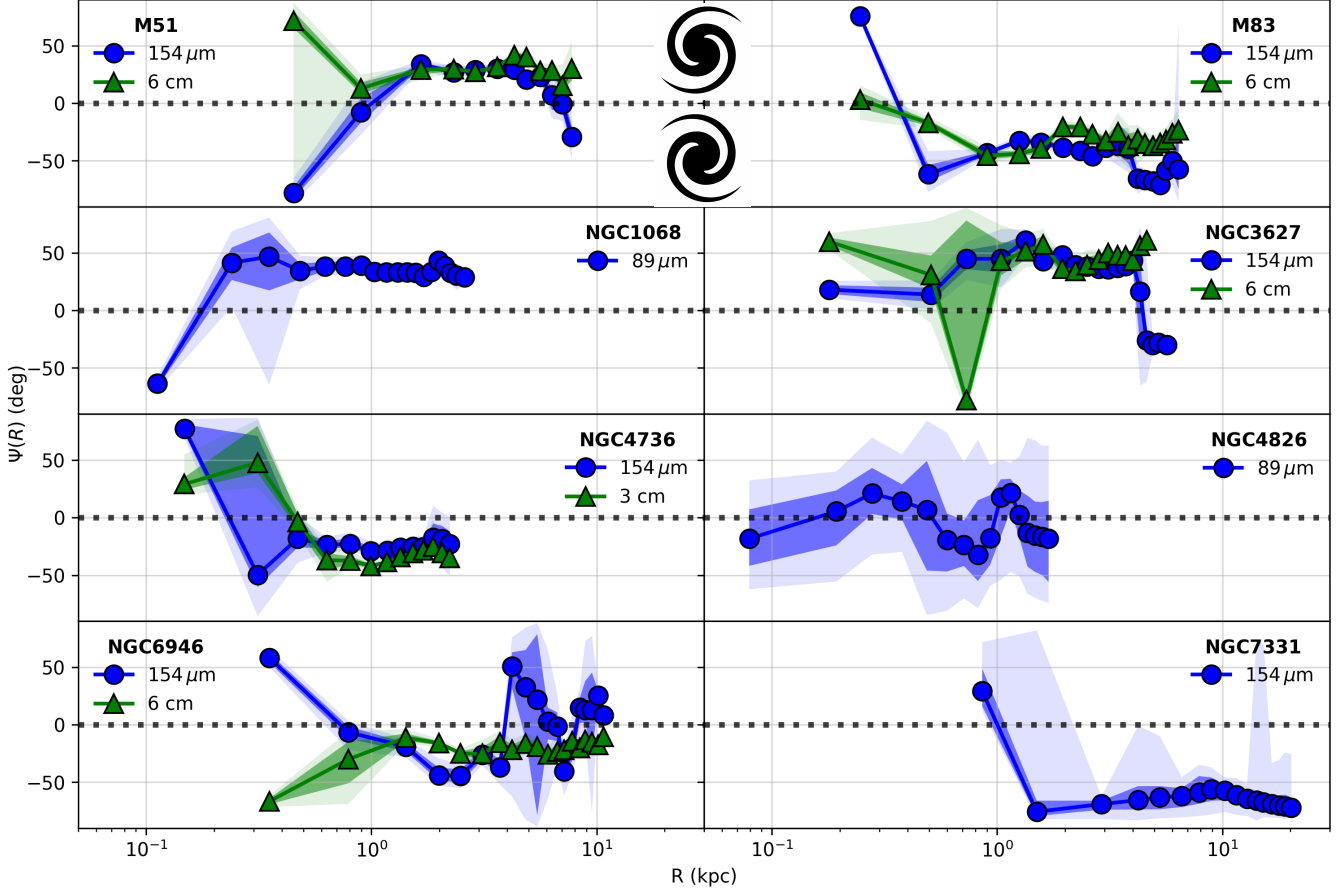


Figure 9. Radial profiles of the magnetic pitch angle (Ψ_B) of spiral galaxies at FIR (blue) and radio (green) wavelengths. The 68% (1σ) and 95% (2σ) statistical significance error contours are shown as shadowed areas.

1068 ($\overline{\Psi_B} = 33.23^{+0.43}_{-0.13}$ at $89\ \mu\text{m}$) has a magnetic pitch angle that is more tightly wound with increasing galactocentric radius ($\rho = -0.618$, $p = 0.006$, Spearman correlation test).

In summary:

- FIR and radio wavelengths do not generally trace the same B -field morphology in spiral galaxies.
- Magnetic pitch angle profiles traced with radio polarization observations present a more constant distribution than those obtained with FIR (i.e., the outskirts of M 51, M 83, or the entire disk of NGC 6946).
- NGC 6946 has a large-scale well-ordered spiral B -field at radio wavelengths, while the B -field is highly disordered at FIR wavelengths. The FIR polarization is mainly cospatial with the star-forming regions, while the radio polarization is cospatial with the morphological interarm regions.

5. ANGULAR DISPERSION

5.1. Methodology

In addition to the magnetic pitch angle, *Mohawc* calculates the residuals between the magnetic pitch angle model and the measured B -field orientation maps. This is intended to provide a quantitative measurement of the goodness-of-fit for the axisymmetric spiral B -field model. By doing so, we can determine which regions are dominated by large-scale ordered spiral magnetic fields (low residuals) or by ‘disordered’ B -fields (high residuals). Note that we use the term ‘disordered’ rather than turbulent B -fields, because ‘turbulent’ is typically defined as the coherence length of the B -field in the ISM of 50 – 100 pc (Ruzmaikin et al. 1988; Brandenburg & Subramanian 2005; Haverkorn et al. 2008a). These scales are well-below the physical resolution, $\theta_{\text{beam,pc}} = [210, 1025]$ pc (Table 3), of the FIR and radio observations of spiral galaxies, and hence cannot contribute to polarized emission. We define the magnetic alignment parameter, ζ , as:

$$\zeta = \cos 2\delta\theta \quad (3)$$

Table 4. Magnetic pitch angles. *Columns, from left to right:* (a) Galaxy name. (b) FIR wavelength. (c) FIR magnetic pitch angle. The errors represent the standard deviation of the pitch angle profile, not the uncertainties of the average value. (d) Average ζ alignment of the FIR spiral magnetic field. (e) Radio wavelength. (f) Radio magnetic pitch angle. (g) Average ζ alignment of the radio spiral magnetic field. (h) Difference in ζ alignment between the radio and FIR spiral magnetic field.

Galaxy	Band	$\langle\Psi_B^{\text{FIR}}\rangle$	ζ^{FIR}	Band	$\langle\Psi_B^{\text{Radio}}\rangle$	ζ^{Radio}	$\Delta\zeta^{\text{Radio-FIR}}$
(a)	(b)	(c)	(d)	(e)	(f)	(g)	(h)
	(μm)	($^\circ$)	(%)	(cm)	($^\circ$)	(%)	(%)
Centaurus A	89	-	-	-	-	-	-
Circinus	53, 89, 154	-	-	-	-	-	-
M51	154	$28.2^{+1.3}_{-40.5}$	$88.7^{+1.2}_{-1.2}$	3 cm	$29.80^{+10.7}_{-5.6}$	$95.28^{+0.62}_{-0.96}$	$+6.4^{+3.0}_{-2.4}$
				6 cm	$29.8^{+10.7}_{-5.6}$	$94.31^{+0.85}_{-0.45}$	$+7.8^{+2.9}_{-2.5}$
M82	53, 89, 154, 214	-	-	-	-	-	-
M83	154	$-38.4^{+2.3}_{-27.0}$	$80.71^{+0.69}_{-3.4}$	6 cm	$-31.2^{+10.4}_{-6.7}$	$90.5^{+0.5}_{-2.1}$	$+12.7^{+4.2}_{-3.6}$
NGC 253	89, 154	-	-	-	-	-	-
NGC 1068	53	-	-	-	-	-	-
	89	$33.1^{+5.8}_{-2.7}$	$86.4^{+5.1}_{-5.2}$	-	-	-	-
NGC 1097	89, 154	-	-	-	-	-	-
NGC 2146	53, 89, 154, 214	-	-	-	-	-	-
NGC 3627	154	$36.6^{+8.9}_{-63.2}$	$80.97^{+0.16}_{-1.57}$	6 cm	$47.8^{+9.2}_{-12.8}$	$91.93^{+1.16}_{-0.28}$	$+11.0^{+4.8}_{-3.8}$
NGC 4736	154	$-24.9^{+6.8}_{-4.0}$	$93.6^{+0.1}_{-4.7}$	3 cm	$-34.0^{+33.4}_{-3.4}$	$95.83^{+0.01}_{-0.35}$	$+1.7^{+1.5}_{-1.0}$
NGC 4826	89	-6^{+22}_{-12}	$57.7^{+4.7}_{-4.2}$	-	-	-	-
NGC 6946	154	-6^{+40}_{-31}	51^{+18}_{-18}	6 cm	$-17.4^{+2.5}_{-7.0}$	$88.0^{+1.8}_{-3.9}$	$+76.0^{+6.2}_{-6.2}$
NGC 7331	154	$-66.2^{+7.7}_{-4.0}$	$86.62^{+0.31}_{-1.53}$	-	-	-	-

where $\delta\theta$ is defined in Eq. 15 from Clark & Hensley (2019) as the angle difference from two angular measurements, θ_1 and θ_2 ,

$$\delta\theta = \frac{1}{2} \arctan \left[\frac{\sin(2\theta_1) \cos(2\theta_2) - \cos(2\theta_1) \sin(2\theta_2)}{\cos(2\theta_1) \cos(2\theta_2) + \sin(2\theta_1) \sin(2\theta_2)} \right] \quad (4)$$

ζ can range from 1 (perfect alignment) to -1 (perpendicular fields). $\zeta = 1$ thus represents a perfect alignment of the median axisymmetric spiral B -field with the local field (large scale B -field dominates). A random polarization field (disordered dominated) will yield an average value of $\zeta = 0$. Since the axisymmetric model is measured from the polarization maps, $\zeta = -1$ values are not expected unless extreme small-scale local changes in the B -field direction are present.

The ζ radial profiles can be constructed using the same method as the magnetic pitch angle profiles (see Sec. A). We use the pitch angle probability distribution of each pixel to calculate ζ as a function of the galactocentric radius and the associated uncertainties (68%, 95%, equivalent to the 1σ , 2σ). For all the analyses, we consider a critical level of at least $p = 0.05$ (95%) to declare statistical significance. This method is implemented in PYTHON and is available on the

project website. Most of the large ζ regions are usually at the cores as expected given the limited statistics within the central 2-3 beams. Low alignment for the inner beams can be caused both by statistical limitations (low number of valid pixels at the core), observational limitations (beam depolarization), and intrinsic physical properties of the core (higher turbulence). We remove the central 2-3 beams for the analysis.

5.2. Results

Figure 10 shows the ζ maps of spiral galaxies on a pixel-by-pixel basis at FIR and radio wavelengths. Fig. 11 presents the ζ profiles of magnetic alignment as a function of galactocentric radius for all spiral galaxies in FIR and radio when available. To compare the magnetic alignment profiles as a function of wavelength, we show the histograms of the difference between radio and FIR, calculated as the difference between the ζ maps from Fig. 10. The median and 1σ uncertainty of the histogram are shown in each plot and Table 4.

We find a mostly flat and high $\zeta > 0.8$ across the full disk of the spiral galaxies in both FIR and radio wavelengths (Fig. 11). This result indicates that a large-scale axisymmetric ordered B -field is the dominant B -field structure in the

Table 5. General variation of the magnetic field pitch angle with increasing galactocentric radius. The following symbols indicate the increase (+), decrease (−), constant (=), or high angular dispersion (!) of Ψ vs. R for the different polarization bands. *Columns, from left to right:* (a) Galaxy name. (b) HAWC+ band (c) FIR Ψ vs. R (d) Radio band (e) Radio Ψ vs. R

Galaxy	FIR band	FIR Ψ vs. R	Radio band(s)	Radio Ψ vs. R
(a)	(b)	(c)	(d)	(e)
M 51	D	−	3, 6	+
M 83	D	−	6	−
NGC 1068	C	−		
NGC 3627	D	+	6	+
NGC 4736	D	=	3	−
NGC 4826	C	44		
NGC 6946	D	!	6	−
NGC 7331	D	44		+

disk of galaxies at both FIR and radio wavelengths, although the individual ζ measurements at the two wavelength regimes may differ.

The ζ profiles in Fig. 11 show that in all analyzed spiral galaxies with radio and FIR data, the magnetic alignment at FIR wavelengths is systematically lower than at radio wavelengths at the same radii. We quantify this result by analyzing the difference between radio and FIR alignment maps ($\Delta\zeta$, % increase of ζ_{FIR} over ζ_{Radio}) in Fig. 12. The average values of ζ are always statistically larger in radio polarization observations than FIR when compared in the same beams. The histograms show that M 51, M 83, NGC 3627, NGC 4736, and NGC 6946 have a better alignment with the large-scale ordered B -field in radio than in FIR ($\Delta\zeta = [2 - 75]\%$, radio - FIR). We show the average differences $\Delta\zeta$ for each galaxy in Table 4, and we confirm that all of them are statistically significant ($p < 10^{-4}$). This suggests that the disordered component of the B -field within the beam (i.e., small-scale B -fields) of observations at FIR wavelengths may have a larger contribution than at radio wavelengths.

In summary:

- Spiral galaxies have a dominant, $\zeta > 0.8$, large-scale axisymmetric spiral B -field in both radio and FIR wavelengths.
- Radio polarization show larger ζ (more ordered B -fields) than those from FIR polarization measurements (more disordered B -fields). Specifically, the FIR B -fields have 2 – 75% more disordered B -fields than those measured at radio wavelengths.

6. DISCUSSION

Magnetic fields extending over kpc-scales have been detected in many spiral galaxies using IR and radio-polarization observations (Beck & Gaensler 2004; Beck 2015a). These B -fields are a fundamental part of galaxy evolution, driving gas mass inflows into the galactic core (Kim & Stone 2012), regulating the star formation rate through the removal of angular momentum in contracting proto-stellar gas clouds (Mouschovias & Ciolek 1999; Allen et al. 2003; Dapp & Basu 2010; Pattle et al. 2022), affecting the formation of molecular clouds (Tahani et al. 2022a,b; Abe et al. 2021), and even potentially affecting the global morphology and gas kinematics in disk galaxies (Battaner & Florido 2007; Ruiz-Granados et al. 2010; Martin-Alvarez et al. 2020; van de Voort et al. 2021). In spite of the substantial research efforts, the formation and structure of kpc-scale B -fields in galaxies, as well as their possible role in the evolution of their hosts, are still outstanding questions in modern astrophysics.

The magnetic fields in spiral galaxies are observed to generally follow spiral patterns resembling the morphological spiral arms (Beck et al. 2019; Lopez-Rodriguez et al. 2020b). This spatial correlation is in agreement with the current paradigm in which weak seed magnetic fields (Rees 1987; Subramanian 2016) are amplified by dynamo mechanisms such as small-scale ($< 50\text{--}100$ pc) turbulence (Beck 1996; Brandenburg & Ntormousi 2022; Haverkorn et al. 2008b; Bhat et al. 2016; Martin-Alvarez et al. 2022), and then reorganize them through differential galactic disk rotation and helical turbulence (large-scale dynamos, Gressel et al. 2008a,b; Gent 2012; Bendre et al. 2015; Ntormousi et al. 2020).

While turbulent dynamos efficiently convert turbulent kinetic energy into magnetic energy (Widrow 2002; Kulsrud & Zweibel 2008; Federrath 2016; Rincon 2019), amplification takes place at the smallest scales and the resulting magnetic field follow the isotropic character of the driving turbulent field. The observations of kpc-scale magnetic field structures in spiral galaxies (Beck et al. 2019; Lopez-Rodriguez et al. 2020b; Borlaff et al. 2021) thus suggest that small-scale dynamos do not operate alone. Theoretical and modeling studies suggest that the efficient small-scale dynamos provide strong seed B -fields for other less-efficient large-scale ordering mechanisms (i.e. differential rotation), which would subsequently align the field (Lou & Fan 1998; Arshakian et al. 2009; Bhat et al. 2016). In addition to differential rotation, the interaction between small-scale dynamos and spiral density waves has been proposed as a mechanism for ordering the magnetic field in spiral galaxies (Beck & Wielebinski 2013). Spiral density waves (Lin & Shu 1964; Bertin & Lin 1996; Sellwood 2011; Dobbs & Baba 2014; Font et al. 2019) periodically compress and shear the interstellar medium (ISM), triggering star formation in their wake. Spiral density waves can also modulate parameters of the large scale dynamo and lead to enhanced non-axisymmetric fields (anti-) correlated with the spiral (Mestel & Subramanian 1991; Shukurov 1998; Chamandy et al. 2013). As density waves travel through the ISM, magnetic field lines are

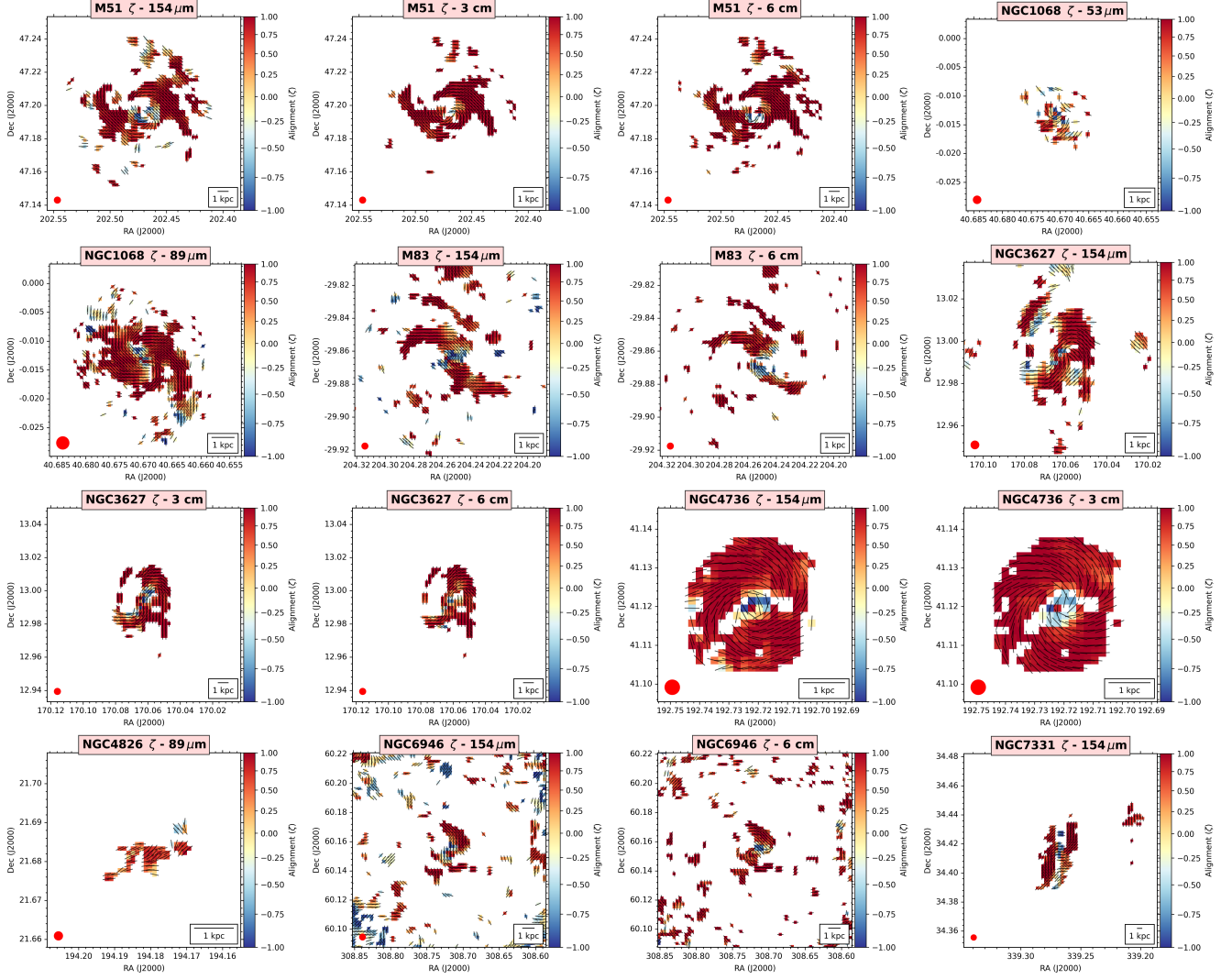


Figure 10. Disordered-to-ordered B -field ratio (magnetic alignment; ζ) maps at FIR and radio wavelengths of spiral galaxies. The measured (black dashes) B -field orientations are shown. Maps are shown with pixels at the Nyquist sampling (Table 1).

sheared along the direction of the spiral arm, aligning the field with the morphological arms.

The mechanism described above to form kpc-scale ordered galactic magnetic fields scenario would work efficiently in grand-design spiral galaxies like M 51 (Patrikeev et al. 2006) or M 83 (Frick et al. 2016b), where star formation takes place preferentially on the spiral arms. Flocculent spirals (i.e., NGC 253, NGC 6946) would be less affected by the spiral density arm shear compression and as a consequence, they might present less ordered spiral magnetic fields, or lower alignment with their morphological counterparts (see NGC 6946). Similar results should apply to starburst galaxies (e.g., M 82), while AGN-dominated (e.g., Circinus), interacting, or recent merger galaxies (like the Antennae galaxies or Centarus A, Chyży & Beck 2004; Lopez-Rodriguez 2021b) may, in addition, present shock or AGN-induced aligned magnetic fields (Lopez-Rodriguez et al. 2021b).

One of the most striking results from this work is the differences on the patterns and angular dispersions between the FIR and radio B -fields shown in spiral and starburst galaxies. We will discuss these differences in terms of the intrinsic nature of the tracer and the B -field components, and separating the large- and small-scale B -fields.

6.1. FIR vs. Radio magnetic pitch angles in spiral galaxies

We found that the orientation of the large-scale spiral B -fields traced through FIR polarimetric observations is statistically different from those measured through radio-synchrotron polarization observations. Note that radio observations were convolved and rebinned to the angular resolution ($13''6$) of the HAWC+ observations. These results confirm the conclusions from Borlaff et al. (2021, SALSA I) in M51 and extends the result to a larger and more diverse sample of galaxies. We showed that a large-scale ordered spiral B -field is the dominant B -field pattern for both radio and FIR

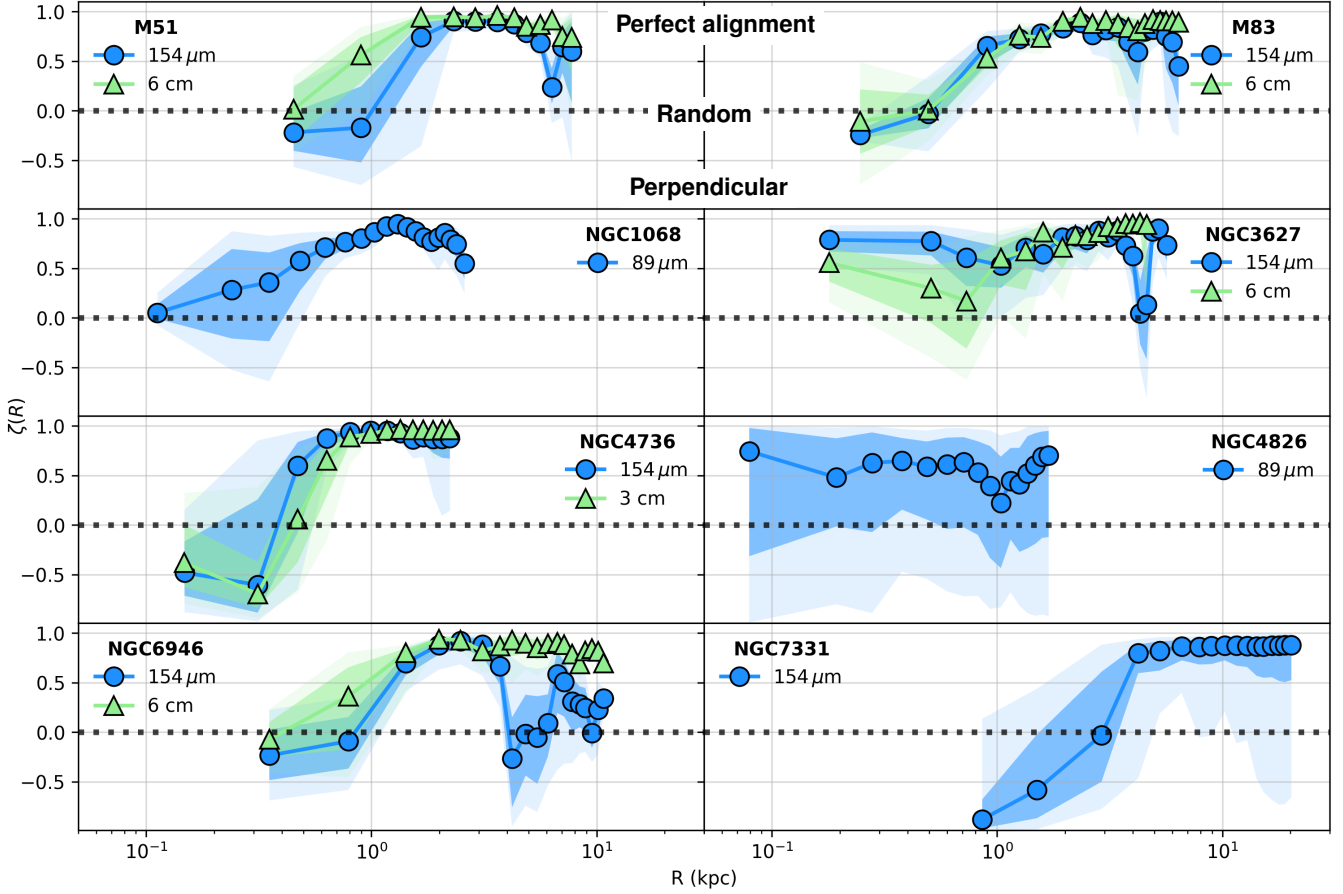


Figure 11. Radial profiles of the magnetic alignment parameter ζ , of spiral galaxies at FIR (blue) and radio (green) wavelengths. $\zeta = +1$ corresponds to a perfect axisymmetric spiral alignment. $\zeta = 0$ corresponds to a completely random B -field. $\zeta = -1$ corresponds to a perpendicular alignment to the average B -field. The 68% (1σ) and 95% (2σ) statistical significance error contours are shown as shadowed areas.

wavelengths (with the exception of NGC 6946). However, the magnetic pitch angle profiles traced with radio polarization observations present a more ordered distribution across the entire disk than those obtained with FIR (i.e., the outskirts of M51, M83, or the entire disk of NGC 6946). Specifically, the radio and FIR magnetic pitch angles show median angular dispersion of 8° and 18° , respectively across the disk of spiral galaxies. In addition, the radio magnetic pitch angle is more open (i.e. larger pitch angles) with increasing galactrocentric radius, while the FIR pitch angle tends to be wrapped tighter (i.e. smaller pitch angles) in the outskirts of spiral galaxies.

Among the potential causes for these B -field morphological differences we consider the intrinsic nature of the B -field tracer. FIR polarization observations trace the B -fields in the cold, $T_d = [19, 48]$ K, and dense, $\log_{10}(N_{\text{HI}+\text{H}_2}[\text{cm}^{-2}]) = [19.9, 22.9]$, ISM (SALSA IV, Lopez-Rodriguez et al. 2022a). The measured FIR polarization is weighted by a combination of density, temperature, and grain alignment efficiency along the LOS and within the beam. Furthermore, the total FIR emission of galaxies has a typical vertical height

of 0.1–0.6 kpc (Verstappen et al. 2013). Thus, the FIR B -fields are sensitive to the morphology and physical conditions of the dense ISM in the central few hundred pc of the galactic disk.

Radio synchrotron polarization traces the B -field in a volume-filling medium of the warm and diffuse ISM (Beck et al. 2019). In spiral galaxies, the radio B -field morphology is observed to have a component parallel to the midplane of the disk and another component with an X-shaped structure extending several kpc above and below the disk (Hummel et al. 1988; Krause et al. 2020). Larger radio halos containing B -fields and cosmic rays are found in galaxies with higher star formation rate surface densities (Wiegert et al. 2015). In addition, radio polarimetric observations suffer from Faraday rotation along the LOS. Radio B -fields are sensitive to the gradient of Faraday rotation (Sokoloff et al. 1998) and the physical conditions of both the halo and the galactic disk, but at 3 and 6 cm this effect is expected to be very small (less than $\pm 5^\circ$ rotation at 3 cm and less than $\pm 20^\circ$ at 6 cm).

Furthermore, the large-scale dynamo (incorporating differential rotation) in galaxies can generate spiral B -fields over

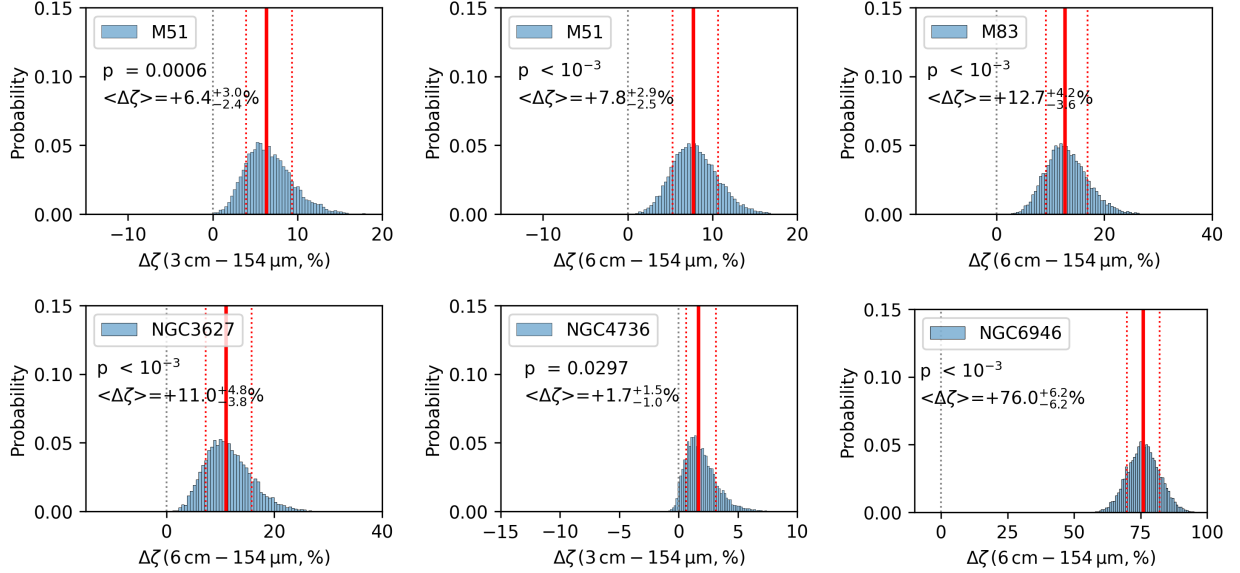


Figure 12. Difference between radio and FIR spiral magnetic alignment parameter ζ of spiral galaxies. The median difference $\Delta\zeta$ (solid red line) and 1σ uncertainty (dashed red line) for each histogram are shown in the top right of each panel (Table 4). The statistical p -value for the null hypothesis that $\Delta\zeta < 0$ is shown in the panel.

kpc-scales (Beck 1996; Gressel et al. 2008a,b) with similar pitch angles to those of the morphological spiral arms (Beck & Wielebinski 2013). Although an offset between the B -fields and the spirals has been measured depending on the tracer (Beck et al. 2019). The large-scale dynamo could operate most efficiently in interarm regions because it may be suppressed or disturbed in the spiral arms (Beck 2015b). The B -field associated with the dense (e.g., molecular) gas may respond in relatively short time-scales to gravitational and kinematic effects like minor mergers, accretion of intergalactic material, and resonances. Diffuse (e.g., HI) gas also responds collisionally, but its scale-height is significantly higher, and its structure is more affected by supernovae explosions and galaxy-scale processes, such as tidal interactions, bar, or spiral formation. Observational effects compatible with these hypotheses have been measured in several galaxies: in the outskirts of M 51 (SALSA I, Borlaff et al. 2021) due to the interaction with M51b. Also in the central starburst of NGC 1097 (SALSA II, Lopez-Rodriguez et al. 2021c), where the radio B -field has a spiral shape following the diffuse gas and the FIR B -field is cospatial with a galactic shock at the boundaries of the bar and the starburst ring. Finally, in the relic spiral arm of the Antennae galaxies (SALSA VI, Lopez-Rodriguez et al. 2022b), where the radio B -field is radial and cospatial with the HI gas dynamics, and the FIR B -field is spiral and cospatial with the dense and molecular ISM.

We suggest that the differences of the radial magnetic pitch angles at radio and FIR wavelengths may be caused by the ‘averaging’ of the several components of the B -fields along the LOS due to the different nature of the two tracers. The FIR magnetic pitch angle traces the B -field in the midplane of the galaxy independently of the distance from the core.

Angular variations of the FIR magnetic pitch angle are driven by the dense ISM and star-forming regions (Section 6.2). However, the radio magnetic pitch angle may be more sensitive to the extraplanar B -field as the distance from the core increases. This may occur by the combination of a) an increase of the vertical height of the X-shaped B -field above and below the disk as galactocentric distance increases, b) an increase of the polarized flux from the X-shaped structure than from the disk, and/or c) depolarization in the arms due to an increase of random turbulent B -fields. We conclude that the FIR and radio magnetic pitch angles trace similar B -fields in the midplane of the disk within the central few kpc of spiral galaxies. However, the radio pitch angle may be arising from different vertical heights as galactocentric radius increases. Specifically, the radio B -field may be extra-planar above the disk along the LOS, while the FIR is co-located with the midplane of the disk at large galactocentric radii.

6.2. Disordered-to-ordered B -fields at FIR and radio

We have introduced the magnetic alignment parameter ζ as a proxy of the disordered-to-ordered B -field ratio on a pixel-to-pixel basis (see Sec. 5.1). The analysis of the ζ alignment maps allowed us to compare the disordered-to-ordered B -field ratio difference between FIR and radio polarimetric observations. Our results indicate that spiral galaxies have a dominant large-scale B -field with a $\zeta > 0.8$ across their disk. We found that the FIR B -field is 2 – 75% more disordered than the radio B -field across the galaxy disk.

Individual measurements with $\zeta \neq 1$ indicates that angular dispersion may be due to a) B -field variations below the physical scale of the beam of the observations, and/or b) B -field variations from some physical mechanisms larger than the physical scale of the beam of the observations.

For the latter, systematic angular dispersion across several beams are expected, while random angular dispersion between beams can indicate the signature of small-scale B -fields. The azimuthally-averaged ζ radial profiles, $\zeta(R)$, allow us to identify the variation of the disordered-to-ordered magnetic field in the spiral galaxies of our sample. Variations of $\zeta(R)$ indicates deviations from the axisymmetric large-scale ordered B -field at scales larger than the beam of the observations. Angular variations larger than the beams of our observations can be driven by tangled random B -fields, B -field instabilities (Parker loops), and/or gas dynamics due to winds, outflows, supernovas, galaxy dynamics, or galaxy interactions. Angular variations smaller than the beam of our observations can be driven by tangled random B -fields due to star-formation, supernovas, or molecular clouds, increase of gas turbulence due to galaxy interaction or gas dynamics.

Lopez-Rodriguez et al. (2022a, SALSA IV) analyzed the trends of the FIR polarization fraction with the column density as a proxy to estimate the random B -fields in the ISM. SALSA IV showed that the spiral galaxies have a relative increase of isotropic random FIR B -fields driven by star-forming regions in the spiral arms. Section 6.1 have shown that the FIR and radio polarized emission trace different components of the B -field in the disk of galaxies. In addition, $\Delta\zeta$ showed that the FIR B -field has is 2 – 75% more disordered than the radio B -field as measured by the independent measurements of ζ . These results suggest that the B -field observations associated to dense, dusty, star-forming regions are less ordered than warmer, less-dense regions of the ISM.

FIR observations of molecular clouds in the Milky Way showed that the B -field orientation can be drastically different as a function of the density of the ISM (Pillai et al. 2020). It is possible then that observationally, the properties of both the small- and large-scale magnetic fields differ as a function of the tracer and the phases of the ISM (Seta & Federrath 2022). Our results indicate that the FIR polarimetric observations can be used as an indicator of the small-scale B -fields associated to the activity of the star-forming regions and the morphology of the molecular clouds within a vertical height of few hundred pc in the disk of spiral galaxies. In addition, $\zeta(R)$ also shows that the FIR B -fields have larger fluctuation across the disk than radio B -fields. This result may indicate that FIR polarization is more sensitive to large-scale mechanisms (i.e. outflows, Parker loops, galaxy interaction) affecting the galaxy.

6.3. Starburst galaxies

The differences between the magnetic field traced by FIR and radio polarimetric observations are even more striking in our sub-sample of starburst galaxies (M 82, NGC 253, and NGC 2146). We found that FIR polarimetric observations are able to trace the B -field by means of magnetically aligned dust grains along the galactic outflows within the 53 – 214 μm wavelength range.

For M82, we estimate a strong change of the average magnetic field position angle ($\langle PA_B^{\text{hist}} \rangle$ and $\langle PA_B^{\text{int}} \rangle$) with wavelength in both FIR (from $\sim 150^\circ$ in 53 μm to $\sim 60^\circ$ in

214 μm), and radio ($\sim 90^\circ$ in 6 cm, see Figure 7 and Table 6). The radio polarimetric observations trace the B -field by means of synchrotron emission in a magnetized bar mostly coincident with the galactic disk (Adebahr et al. 2013, 2017). A similar conclusion can be obtained from the observations of NGC 253 (Heesen et al. 2011). While the inner regions show B -field orientations parallel to the disk of the galaxy in all wavelengths, strong discrepancies are observed in the outskirts, which might be a signature of galactic outflows. Although some Faraday depolarization may be affecting the radio polarimetric observations, we suggest that the discrepancy may be produced by the limited lifetime of the cosmic rays (CR) along the galactic outflows. This may be explained by the weak total synchrotron emission in the outflow (Adebahr et al. 2013, fig. 6). In addition, the steep spectral indexes may be an indication of rapid aging of the CR electrons. FIR total intensity observations with *Herschel* have shown ~ 10 kpc scale extensions of dust above and below the disk (Roussel et al. 2010). The galactic outflow may have expelled $\geq 25\%$ of the total dust mass of the galaxy (Roussel et al. 2010), making the cold phase of the ISM to be the bulk of the mass along the galactic outflow. Thus, the B -field along the galactic outflows of starburst galaxies are better traced by using FIR polarimetric observations.

Radio polarimetric observations have measured an X-shaped structure extending several kpc above the disks of edge-on spiral galaxies (Krause et al. 2020). This vertical B -field is different to that observed here in starburst galaxies. Our FIR polarimetric observations in edge-on galaxies do not show signs of a X-shaped B -field structure. This is expected as the vertical height of dust emission is 0.1 – 0.6 kpc (Verstappen et al. 2013), while the X-shaped B -field observed in radio corresponds to synchrotron polarized emission from warm gas in the halo at several kpc scales.

FIR polarimetric observations also reveal strong structural differences of the B -field with wavelength in the 53 – 214 μm range, as observed in Circinus (Fig. 2) and NGC 2146 (Fig. 5). For Circinus, the 53 μm and 89 μm B -fields may be dominated by the starburst ring and the inner-bar, while the 214 μm B -field may be tracing the B -field in the outer bar and spiral arms of the host galaxy (Maiolino et al. 2000; Izumi et al. 2018). Further modeling is required to quantify these results.

The most extreme case is NGC 2146. This galaxy shows a B -field with an orientation perpendicular to the galactic disk in the 53 – 89 μm wavelength range associate with the galactic outflow. The 214 μm observations reveal a parallel B -field to the galactic disk associated to the galactic B -field. Lopez-Rodriguez et al. (2022a, SALSA IV) computed the polarized spectral energy distribution (SED) of starburst galaxies showing a minimum within the 89 – 154 μm wavelength range. The falling 53 – 154 μm polarized spectrum was suggested to be produced by a decrease in the dust grain alignment efficiency due to a gradient of dust temperatures along the LOS. The rise spectrum at 154 – 214 μm was suggested to be produced by the dust becoming more optically thin at larger wavelengths. Thus, the measured 154

μm B -field orientation is expected to be the transition between the two regimes (see Sec. 3.2.1). In addition, the extremely complex morphological structure of NGC 2146 suggests that it is the remnant of a recent interaction that triggered star-formation bursts (Martini et al. 2003; Tarchi et al. 2004; Erwin 2005). While it is beyond the scope of this paper to explore this, the B -field orientation differences detected within the different SOFIA HAWC+ bands suggest that FIR polarized emission could be dominated by different populations of dust grains as a function of wavelength, revealing different physical regimes in terms of density, radiation, or turbulence.

7. CONCLUSIONS

The HAWC+/FIR polarimetric observations of the SALSALSA Legacy Program of 14 nearby (< 20 Mpc) galaxies analyzed in this paper, and presented in the previous publications from the project (SALSALSA I – IV) provide a previously unexplored view of a fundamental factor in galaxy evolution: the B -fields in the dense and cold ISM of galaxies. While galactic B -fields have been observed for decades in radio polarization observations, high-spatial resolution FIR maps from molecular clouds in the Milky Way (i.e., Pillai et al. 2020) demonstrate that the structure of magnetic fields is a strong function of the density of the ISM at scales of hundreds of pc.

Here, we provide quantitative evidence that the kpc-scale of galactic magnetic fields depends strongly of the tracer, in this case radio polarization observations of the synchrotron emission at 3 and 6 cm, or FIR polarization observations of the thermally aligned dust grains. In addition, we introduce the new alignment parameter (ζ , Sec. 5), as a quantitative measure of the dispersion of a spiral magnetic field, allowing to estimate how well-ordered a spiral magnetic field is, and to compare as a function of different observational tracers.

Our results suggest that radio and FIR polarization observations do not necessarily trace the same magnetic field structures. For most of our galaxies, significant differences are found in terms of local and global orientation of the magnetic field (Sec. 3.2), the pitch angle of spiral galaxies (Sec. 4), and the dispersion of the magnetic spiral structure (Sec. 5.2). We find evidence that even FIR polarization observations can trace different structures of the magnetic field as a function of wavelength as observed in NGC 2146 ($53 \mu\text{m} - 214 \mu\text{m}$, see Fig. 5). The differences in the magnetic pitch angle profiles (Fig. 9), and the alignment ζ maps (Figs. 9) indicate that radio polarization observations tend to trace a more regular and stable structure of the magnetic field, with less variation of the magnetic pitch angle, and a higher level of alignment ζ . None of the five spiral galaxies studied with available FIR and radio polarization observations presented a lower ζ alignment in radio than in FIR, and three of them (M 51, M 83, NGC 6946) presented a statistically higher magnetic field dispersion in FIR than in radio (see Fig. 12).

While our observations are limited by spatial resolution and thus not able to resolve individual molecular clouds, all results point towards the conclusion that FIR polarization observations trace a less-ordered structure of the magnetic

field than radio polarization observations. We suggest that FIR polarization observations are dominated by the emission from magnetically aligned dust grains cospatial with the cold, dense ISM, while radio polarization observations trace more diffuse regions of the ISM, less dominated by kinematic turbulence. Each beam from both radio and FIR polarization maps would be tracing an average of the magnetic field inside them, but dominated by the the dense, dusty molecular clouds in FIR. Star-formation, outflows, and accretion, and the morphological complexity of the galactic filaments of dust would increase the dispersion of the magnetic field from the average kpc-scale magnetic field orientation, with a lower effect on less-dense phases of the ISM.

High-resolution, FIR polarization observations of galaxies such as those provided by SOFIA/HAWC+ until its last flight in September 2022 are vital to understand the role of magnetic fields in the evolution of the Universe. While facilities like ALMA, South Pole Telescope, or James Clerk Maxwell Telescope provide observations in sub-millimetric and/or FIR wavelength ranges, they lack the sensitivity, spatial resolution, or polarimetric capabilities in the required wavelengths to achieve the same scientific requirements in nearby galaxies. In the absence of facilities such as SOFIA or SPICA, unique in their ability to investigate the dusty component of galaxies as well as their magnetic fields, the astronomical community has no current alternatives to explore the magnetic fields inside the dust component of nearby galaxies through FIR polarimetry. Only the support of the astronomical community through proposed missions like PRIMA (Bradford et al. 2022, potential launch no earlier than 2030) for the upcoming NASA far-infrared (FIR) Probe missions or future FIR polarimetric missions will ensure a continuation of this field in the next decades.

Facilities: SOFIA (HAWC+), ALMA, *Herschel*, VLA.

Software: ASTROPY ([Astropy Collaboration et al. 2013](#)), APLPY ([Robitaille & Bressert 2012](#)), MATPLOTLIB ([Hunter 2007](#)),

1 Based on observations made with the NASA/DLR Strato-
 2 spheric Observatory for Infrared Astronomy (SOFIA) under
 3 the 07.0034, 08.0012 Program. SOFIA is jointly operated by
 4 the Universities Space Research Association, Inc. (USRA),
 5 under NASA contract NNA17BF53C, and the Deutsches
 6 SOFIA Institut (DSI) under DLR contract 50 OK 0901 to
 7 the University of Stuttgart. KT has received funding from
 8 the European Research Council (ERC) under the European
 9 Unions Horizon 2020 research and innovation programme
 10 under grant agreement No. 771282

11 A.B. acknowledges the incredible support and tireless ef-
 12 fort from Christine Martinez (NASA/Ames STA), that made
 13 this work possible. A.B. was supported by an appointment
 14 to the NASA Postdoctoral Program at the NASA Ames Re-
 15 search Center, administered by Oak Ridge Associated Uni-
 16 versities under contract with NASA. A.B. is supported by
 17 program Hubble Archival Research project AR 17041, and
 18 Chandra Archival Research project ID #24610329, provided
 19 by NASA through a grant from the Space Telescope Science
 20 Institute and the Center for Astrophysics Harvard & Smith-
 21 sonian, operated by the Association of Universities for Re-
 22 search in Astronomy, Inc., under NASA contract NAS 5-
 23 03127.

24 M. Tahani is supported by the Banting Fellowship (Natural
 25 Sciences and Engineering Research Council Canada) hosted
 26 at Stanford University and the Kavli Institute for Particle As-
 27 trophysics and Cosmology (KIPAC) Fellowship. IMC ac-
 28 knowledges funding from University of La Laguna through
 29 the Margarita Salas Fellowship from the Spanish Ministry
 30 of Universities ref. UNI/551/2021-May 26, and under the
 31 EU Next Generation funds. This research was sponsored by
 32 the National Aeronautics and Space Administration (NASA)
 33 through a contract with ORAU. The views and conclusions
 34 contained in this document are those of the authors and
 35 should not be interpreted as representing the official poli-
 36 cies, either expressed or implied, of the National Aeronau-
 37 tics and Space Administration (NASA) or the U.S. Govern-
 38 ment. The U.S. Government is authorized to reproduce and
 39 distribute reprints for Government purposes notwithstanding
 40 any copyright notation herein.

APPENDIX

A. MEASUREMENTS OF THE POLARIZATION ANGLES AT FIR AND RADIO WAVELENGTHS

This section shows the histograms of the B -field orientations at 6 cm. We show the noise levels applied to the polarization maps.

APPENDIX

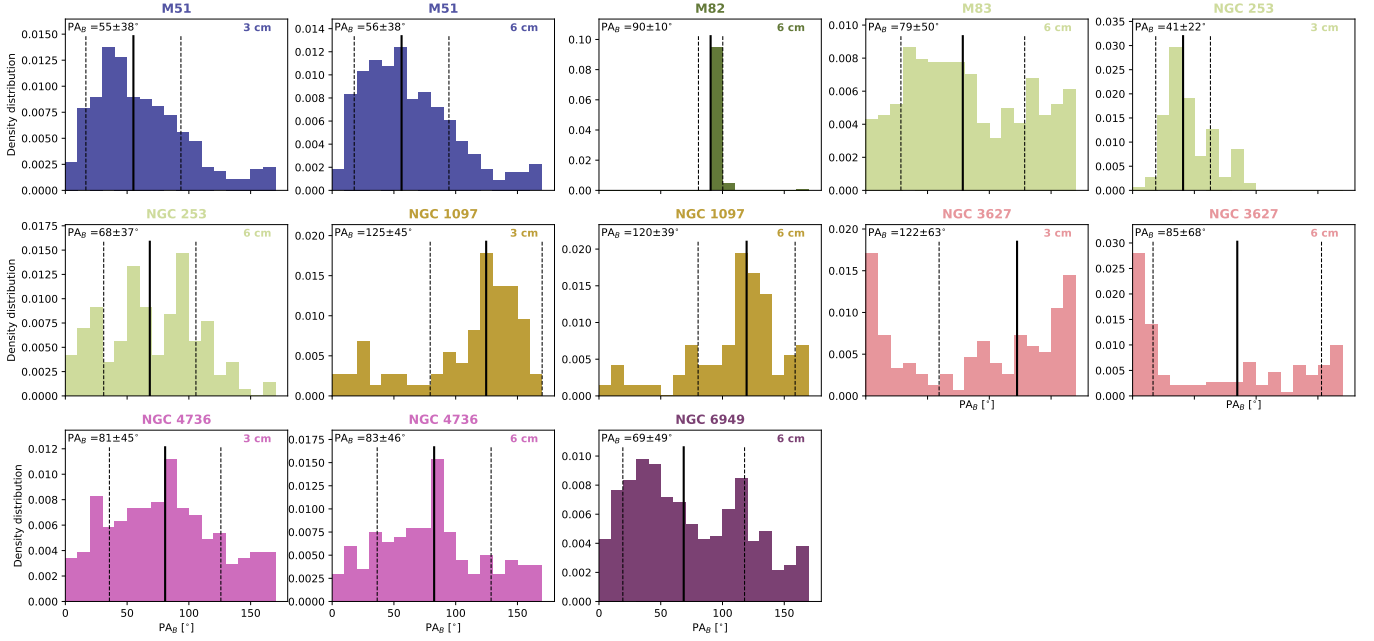


Figure 13. Histograms of the B -field orientations for the galaxies with radio polarimetric observations (Table 2). The histograms are set to 10° bins, each galaxy is shown in a unique color, and the median (black solid line) and 1σ uncertainty (black dashed line) for the radio observations are shown. Given the similarities of the B -field orientations between 3 and 6 cm wavelengths, only the histograms of the B -field orientations at 6 cm are shown in Figure 7.

A. MEASURING THE PITCH ANGLE OF THE FIR AND RADIO POLARIZATION FIELDS

We analyze the magnetic pitch angles of the B -field maps following the methodology (`Mohawc`) presented by Borlaff et al. (2021) on M51. Here, we summarize the steps to estimate the magnetic pitch angle, Ψ_B , as a function of the galactrocentric radius of spiral galaxies. `Mohawc` uses the Stokes IQU maps to derive the Ψ_B profiles on a pixel-per-pixel basis, assuming that all the B -field orientations are on the galactic plane viewed at a certain inclination, i , with respect to the observer, and position angle, θ , on the plane of the sky. The uncertainties of the Stokes IQU , position angle, and inclination are taken into account through Monte Carlo simulations. Our magnetic pitch angle estimation method entails processing the data on a pixel-by-pixel basis, allowing the user to separate different regions of the galaxy by using masks (if desired). The steps followed by `Mohawc` can be summarized as follows:

1. The debiased polarization degree and its associated uncertainty are computed using the Stokes IQU parameters and their uncertainties δI , δQ , δU :

$$P_{\text{debias}} = \sqrt{P^2 - \delta P^2} \quad (\text{A1})$$

following Serkowski (1974), where:

$$P = \sqrt{\left(\frac{Q}{I}\right)^2 + \left(\frac{U}{I}\right)^2} \quad (\text{A2})$$

and:

$$\delta P = \frac{1}{I} \sqrt{\frac{(Q \cdot \delta Q)^2 + (U \cdot \delta U)^2}{Q^2 + U^2} + \delta I^2 \frac{Q^2 + U^2}{I^2}} \quad (\text{A3})$$

2. The B -field orientations are then re-projected to a new reference frame where the galaxy is observed face-on, using coordinates of the galactic center (α , δ), the galactic disk inclination, i , and tilt angle, θ . The morphological parameters for each galaxy are summarized in Table 3.

Table 6. Median and integrated polarization fraction and B -field orientation of galaxies. *Columns, from left to right:* a) Galaxy name, b) central wavelength of the HAWC+ band, c) median polarization angle based on individual measurements at FIR wavelengths d) median polarization angle based on the integrated Stokes IQU of the full galaxy at FIR wavelengths, e) central wavelength of the band at radio wavelengths, f) median polarization angle based on individual measurements at radio wavelengths, g) median polarization angle based on the integrated Stokes IQU of the full galaxy at radio wavelengths.

Galaxy	Band	$\langle PA_{B,FIR}^{hist} \rangle$	$\langle PA_{B,FIR}^{int} \rangle$	Band	$\langle PA_{B,Radio}^{hist} \rangle$	$\langle PA_{B,Radio}^{int} \rangle$
	(μm)	($^\circ$)	($^\circ$)	(cm)	($^\circ$)	($^\circ$)
(a)	(b)	(c)	(d)	(e)	(f)	(g)
Centaurus A	89	121 ± 28	126 ± 9	-	-	-
Circinus	53	53 ± 23	59 ± 13	-	-	-
	89	32 ± 37	30 ± 12	-	-	-
	214	37 ± 77	179 ± 2	-	-	-
M51	154	53 ± 36	56 ± 12	3	55 ± 38	47 ± 1
				6	56 ± 38	53 ± 1
M82	53	145 ± 52	155 ± 4	6	90 ± 10	-*
	89	138 ± 55	153 ± 5	-	-	-
	154	86 ± 43	86 ± 7	-	-	-
	214	61 ± 41	53 ± 3	-	-	-
M83	154	65 ± 40	50 ± 10	6	79 ± 50	44 ± 1
NGC 253	89	57 ± 41	39 ± 19	3	41 ± 22	44 ± 2
	154	61 ± 23	164 ± 56	6	68 ± 37	70 ± 3
NGC 1068	53	108 ± 49	39 ± 84	-	-	-
	89	121 ± 48	135 ± 10	-	-	-
NGC 1097	89	127 ± 32	132 ± 5	3	125 ± 45	134 ± 1
	154	125 ± 35	134 ± 16	6	120 ± 39	128 ± 1
NGC 2146	53	63 ± 16	65 ± 10	-	-	-
	89	75 ± 29	80 ± 9	-	-	-
	154	135 ± 61	160 ± 9	-	-	-
	214	124 ± 20	119 ± 4	-	-	-
NGC 3627	154	87 ± 60	17 ± 19	3	122 ± 63	174 ± 1
				6	85 ± 68	0 ± 1
NGC 4736	154	85 ± 42	88 ± 7	3	81 ± 45	72 ± 1
				6	83 ± 46	71 ± 1
NGC 4826	89	104 ± 31	104 ± 10	-	-	-
NGC 6946	154	111 ± 55	161 ± 11	6	69 ± 49	47 ± 1
NGC 7331	154	122 ± 30	121 ± 6	-	-	-

*Stokes QU were not available.

3. An azimuthal angular mask is created. The azimuthal mask is generated such that the deprojected B -field orientation at each pixel location is perpendicular to the radial direction. We will refer to this idealized field as the *zero pitch angle* field or Ξ .

Table 7. Noise level in total intensity (I) and polarized intensity (PI) and quality cuts of the FIR and radio polarization observations of the galaxies in the sample. *Columns, from left to right:* a) Galaxy name, b) central wavelength of the HAWC+ band, c) total intensity noise level in FIR, d) polarized intensity noise level in FIR, e) central wavelength of the band at radio wavelengths, f) total intensity noise level in radio, g) polarized intensity noise level in radio, h) limiting SNR in polarization intensity, i) limiting polarization fraction, and j) limiting SNR in total intensity chosen for each galaxy in (Lopez-Rodriguez et al. 2021b).

Galaxy	Band	σ_I^{FIR}	$\sigma_{\text{PI}}^{\text{FIR}}$	Band	σ_I^{Radio}	$\sigma_{\text{PI}}^{\text{Radio}}$	SNR _{FIR,PI}	p_{lim}	SNR _{FIR,I}
	(μm)	(Jy arcsec ⁻²)	(Jy arcsec ⁻²)	(cm)	(Jy arcsec ⁻²)	(Jy arcsec ⁻²)		(%)	
(a)	(b)	(c)	(d)	(e)	(f)	(g)	(h)	(i)	(j)
Centaurus A	89	$1.39 \cdot 10^{-4}$	$3.39 \cdot 10^{-3}$	-	-	-	2.5	20	10
Circinus	53	$9.17 \cdot 10^{-4}$	10^{-2}	-	-	-	2.3	20	10
	89	$1.22 \cdot 10^{-4}$	$2.96 \cdot 10^{-3}$	-	-	-	3.0	20	10
	214	$3.72 \cdot 10^{-5}$	$4.74 \cdot 10^{-3}$	-	-	-	2.5	20	10
M51	154	$2.23 \cdot 10^{-5}$	$1.52 \cdot 10^{-3}$	3	$1.75 \cdot 10^{-7}$	$2.32 \cdot 10^{-7}$	3.0	20	10
				6	$2.16 \cdot 10^{-7}$	$2.28 \cdot 10^{-7}$			
M82	53	$6.27 \cdot 10^{-4}$	$6.84 \cdot 10^{-3}$	6	-	-	3.0	20	80
	89	$1.65 \cdot 10^{-4}$	$4.02 \cdot 10^{-3}$	-	-	-	3.0	20	80
	154	$3.57 \cdot 10^{-5}$	$2.46 \cdot 10^{-3}$	-	-	-	3.0	20	20
	214	$3.96 \cdot 10^{-5}$	$5.0 \cdot 10^{-3}$	-	-	-	3.0	20	20
M83	154	$2.57 \cdot 10^{-5}$	$1.78 \cdot 10^{-3}$	6	$2.2 \cdot 10^{-7}$	$2.5 \cdot 10^{-7}$	2.5	20	10
NGC 253	89	$2.80 \cdot 10^{-4}$	$6.52 \cdot 10^{-3}$	3	$4.10 \cdot 10^{-7}$	$4.63 \cdot 10^{-7}$	2.5	10	20
	154	$3.30 \cdot 10^{-4}$	$2.12 \cdot 10^{-2}$	6	$7.88 \cdot 10^{-7}$	$6.13 \cdot 10^{-7}$	2.0	10	20
NGC 1068	53	$6.32 \cdot 10^{-4}$	$7.00 \cdot 10^{-3}$	-	-	-	2.0	10	10
	89	$2.60 \cdot 10^{-4}$	$1.18 \cdot 10^{-3}$	-	-	-	2.0	10	10
NGC 1097	89	$2.16 \cdot 10^{-4}$	$4.98 \cdot 10^{-3}$	3	$4.65 \cdot 10^{-8}$	$1.47 \cdot 10^{-7}$	3.0	10	10
	154	$1.47 \cdot 10^{-4}$	$9.88 \cdot 10^{-3}$	6	$5.41 \cdot 10^{-8}$	$2.00 \cdot 10^{-7}$	2.0	10	10
NGC 2146	53	$4.03 \cdot 10^{-4}$	$4.39 \cdot 10^{-3}$	-	-	-	3.0	20	30
	89	$1.39 \cdot 10^{-4}$	$3.38 \cdot 10^{-3}$	-	-	-	3.0	20	20
	154	$3.27 \cdot 10^{-5}$	$2.25 \cdot 10^{-3}$	-	-	-	3.0	20	20
	214	$2.24 \cdot 10^{-5}$	$2.85 \cdot 10^{-3}$	-	-	-	3.0	20	20
NGC 3627	154	$2.59 \cdot 10^{-5}$	$1.79 \cdot 10^{-3}$	3	$4.33 \cdot 10^{-7}$	$5.10 \cdot 10^{-8}$	2.0	20	40
				6	$1.13 \cdot 10^{-6}$	$8.51 \cdot 10^{-8}$			
NGC 4736	154	$4.74 \cdot 10^{-5}$	$3.22 \cdot 10^{-3}$	3	$6.32 \cdot 10^{-8}$	$6.94 \cdot 10^{-8}$	2.0	20	68
				6	$2.05 \cdot 10^{-8}$	$4.76 \cdot 10^{-8}$			
NGC 4826	89	$1.82 \cdot 10^{-4}$	$4.42 \cdot 10^{-3}$	-	-	-	2.3	20	20
NGC 6946	154	$3.10 \cdot 10^{-5}$	$2.14 \cdot 10^{-3}$	6	$9.02 \cdot 10^{-9}$	$5.94 \cdot 10^{-8}$	2.3	20	20
NGC 7331	154	$2.19 \cdot 10^{-5}$	$1.50 \cdot 10^{-3}$	-	-	-	2.8	20	45

*Stokes QU were not available.

- The magnetic pitch angle at each pixel, $\Psi_B(x, y)$, is calculated as the difference between the measured PAs of the B -field orientation and the Ξ vector field.

5. The magnetic pitch angle profile $\Psi_B(x, y)$ is then averaged at each radius from the core. The radial bins are linearly spaced, and their number is optimized as a compromise between SNR and spatial resolution. The angular average as a function of the galactrocentric radius, R , is performed as follows:

$$\overline{\Psi}_B(R) = \text{atan2} \left(\frac{\langle \cos \Psi_B(x, y) \rangle}{\langle \sin \Psi_B(x, y) \rangle} \right) \quad (\text{A4})$$

where the $\langle \rangle$ operator indicates a robust median value (based on randomized Monte Carlo simulations) and $\overline{\Psi}_B(R)$ is the averaged magnetic pitch angle value for a certain radial bin.

For each galaxy, the process detailed above is repeated 10,000 times, using Monte Carlo simulations to include the uncertainties of the tilt angle, inclination, and the Stokes parameters. We assume that each parameter follows a Gaussian probability distribution, with a standard deviation σ equal to their uncertainties. We use the probability distribution for the pitch angle of each pixel to calculate the median magnetic pitch angle, $\overline{\Psi}_B$ radial profiles, and their uncertainties (68%, 95%, equivalent to the 1σ , 2σ). For all the analyses, we consider a critical level of at least $p = 0.05$ (95%) to declare statistical significance.

Note that one of the limitations of *Mohawc* resides in the estimation of the pitch angle within the central 2-3 beams at the core of the galaxies. This limitation is due to the small number of measurements per annulus to obtain statistically significant measurements of the pitch angles (see Fig. 22 by Borlaff et al. 2021). Our analysis only takes into account the polarization measurements in the galaxy disks after 2 beams (4 pixels diameter) from the core. Systematic errors are expected due to the lack of statistics in regions too close to the center, or affected by internal core phenomena, like rings, bars, or AGNs. NGC 1068, M 83, or M 51 are examples of extreme values on their innermost bins, due to statistics, presenting more acceptable values in the second bin.

REFERENCES

- Abe, D., Inoue, T., Inutsuka, S.-i., & Matsumoto, T. 2021, *ApJ*, 916, 83, doi: [10.3847/1538-4357/ac07a1](https://doi.org/10.3847/1538-4357/ac07a1)
- Adebahr, B., Krause, M., Klein, U., Heald, G., & Dettmar, R. J. 2017, *A&A*, 608, A29, doi: [10.1051/0004-6361/201629616](https://doi.org/10.1051/0004-6361/201629616)
- Adebahr, B., Krause, M., Klein, U., et al. 2013, *A&A*, 555, A23, doi: [10.1051/0004-6361/201220226](https://doi.org/10.1051/0004-6361/201220226)
- Allen, A., Li, Z.-Y., & Shu, F. H. 2003, *ApJ*, 599, 363, doi: [10.1086/379243](https://doi.org/10.1086/379243)
- Arshakian, T. G., Beck, R., Krause, M., & Sokoloff, D. 2009, *A&A*, 494, 21, doi: [10.1051/0004-6361:200810964](https://doi.org/10.1051/0004-6361:200810964)
- Astropy Collaboration, Robitaille, T. P., Tollerud, E. J., et al. 2013, *A&A*, 558, A33, doi: [10.1051/0004-6361/201322068](https://doi.org/10.1051/0004-6361/201322068)
- Battaner, E., & Florido, E. 2007, *Frontiers in Astronomy and Space Sciences*, 328, 92, doi: [10.1002/asna.200610658](https://doi.org/10.1002/asna.200610658)
- Beck, R. 1991, *A&A*, 251, 15
- . 1996, *Nachr. Akad. Wiss. Göttingen II*, 1996, 262
- . 2007, *A&A*, 470, 539, doi: [10.1051/0004-6361:20066988](https://doi.org/10.1051/0004-6361:20066988)
- . 2015a, *A&A*, 24, 4, doi: [10.1007/s00159-015-0084-4](https://doi.org/10.1007/s00159-015-0084-4)
- . 2015b, *A&A Rv*, 24, 4, doi: [10.1007/s00159-015-0084-4](https://doi.org/10.1007/s00159-015-0084-4)
- Beck, R., Chamandy, L., Elson, E., & Blackman, E. G. 2019, *Galaxies*, 8, 4, doi: [10.3390/galaxies8010004](https://doi.org/10.3390/galaxies8010004)
- Beck, R., Fletcher, A., Shukurov, A., et al. 2005, *A&A*, 444, 739, doi: [10.1051/0004-6361:20053556](https://doi.org/10.1051/0004-6361:20053556)
- Beck, R., & Gaensler, B. M. 2004, *NewA*, 48, 1289, doi: [10.1016/j.newar.2004.09.013](https://doi.org/10.1016/j.newar.2004.09.013)
- Beck, R., & Wielebinski, R. 2013, *Magnetic Fields in Galaxies*, ed. T. D. Oswalt & G. Gilmore, Vol. 5, 641, doi: [10.1007/978-94-007-5612-0_13](https://doi.org/10.1007/978-94-007-5612-0_13)
- Bendre, A., Gressel, O., & Elstner, D. 2015, *Frontiers in Astronomy and Space Sciences*, 336, 991, doi: [10.1002/asna.201512211](https://doi.org/10.1002/asna.201512211)
- Bertin, G., & Lin, C. C. 1996, *Spiral structure in galaxies a density wave theory*
- Bhat, P., Subramanian, K., & Brandenburg, A. 2016, *MNRAS*, 461, 240, doi: [10.1093/mnras/stw1257](https://doi.org/10.1093/mnras/stw1257)
- Bland-Hawthorn, J., Gallimore, J. F., Tacconi, L. J., et al. 1997, *Ap&SS*, 248, 9, doi: [10.1023/A:1000567831370](https://doi.org/10.1023/A:1000567831370)
- Borlaff, A. S., Lopez-Rodriguez, E., Beck, R., et al. 2021, *ApJ*, 921, 128
- Borlaff, A. S., Lopez-Rodriguez, E., Beck, R., et al. 2021, *arXiv e-prints*, arXiv:2105.09315. <https://arxiv.org/abs/2105.09315>
- Bradford, C., Glenn, J., Armus, L., et al. 2022, in *American Astronomical Society Meeting Abstracts*, Vol. 54, American Astronomical Society Meeting Abstracts, 304.07
- Brandenburg, A., & Ntormousi, E. 2022, *arXiv e-prints*, arXiv:2211.03476. <https://arxiv.org/abs/2211.03476>
- Brandenburg, A., & Subramanian, K. 2005, *PhR*, 417, 1, doi: [10.1016/j.physrep.2005.06.005](https://doi.org/10.1016/j.physrep.2005.06.005)
- Braun, R., Walterbos, R. A. M., Kennicutt, Robert C., J., & Tacconi, L. J. 1994, *ApJ*, 420, 558, doi: [10.1086/173586](https://doi.org/10.1086/173586)
- Brinks, E., Skillman, E. D., Terlevich, R. J., & Terlevich, E. 1997, *Ap&SS*, 248, 23, doi: [10.1023/A:1000519932279](https://doi.org/10.1023/A:1000519932279)
- Chamandy, L., Subramanian, K., & Shukurov, A. 2013, *MNRAS*, 428, 3569, doi: [10.1093/mnras/sts297](https://doi.org/10.1093/mnras/sts297)
- Chyży, K. T., & Beck, R. 2004, *A&A*, 417, 541, doi: [10.1051/0004-6361:20031778](https://doi.org/10.1051/0004-6361:20031778)

- Chżyży, K. T., & Buta, R. J. 2008, *ApJL*, 677, L17, doi: [10.1086/587958](https://doi.org/10.1086/587958)
- Clark, S. E., & Hensley, B. S. 2019, *ApJ*, 887, 136, doi: [10.3847/1538-4357/ab5803](https://doi.org/10.3847/1538-4357/ab5803)
- Colombo, D., Meidt, S. E., Schinnerer, E., et al. 2014, *ApJ*, 784, 4, doi: [10.1088/0004-637X/784/1/4](https://doi.org/10.1088/0004-637X/784/1/4)
- Crosthwaite, L. P., Turner, J. L., Buchholz, L., Ho, P. T. P., & Martin, R. N. 2002, *AJ*, 123, 1892, doi: [10.1086/339479](https://doi.org/10.1086/339479)
- Daigle, O., Carignan, C., Amram, P., et al. 2006, *MNRAS*, 367, 469, doi: [10.1111/j.1365-2966.2006.10002.x](https://doi.org/10.1111/j.1365-2966.2006.10002.x)
- Dapp, W. B., & Basu, S. 2010, *A&A*, 521, L56, doi: [10.1051/0004-6361/201015700](https://doi.org/10.1051/0004-6361/201015700)
- Dicaire, I., Carignan, C., Amram, P., et al. 2008, *MNRAS*, 385, 553, doi: [10.1111/j.1365-2966.2008.12868.x](https://doi.org/10.1111/j.1365-2966.2008.12868.x)
- Dobbs, C., & Baba, J. 2014, *PASA*, 31, e035, doi: [10.1017/pasa.2014.31](https://doi.org/10.1017/pasa.2014.31)
- Dowell, C. D., Cook, B. T., Harper, D. A., et al. 2010, in *Society of Photo-Optical Instrumentation Engineers (SPIE) Conference Series*, Vol. 7735, Proc. SPIE, 77356H, doi: [10.1117/12.857842](https://doi.org/10.1117/12.857842)
- Elmouttie, M., Haynes, R. F., Jones, K. L., Sadler, E. M., & Ehle, M. 1998a, *MNRAS*, 297, 1202, doi: [10.1046/j.1365-8711.1998.01592.x](https://doi.org/10.1046/j.1365-8711.1998.01592.x)
- Elmouttie, M., Krause, M., Haynes, R. F., & Jones, K. L. 1998b, *MNRAS*, 300, 1119, doi: [10.1046/j.1365-8711.1998.02002.x](https://doi.org/10.1046/j.1365-8711.1998.02002.x)
- Erwin, P. 2005, *MNRAS*, 364, 283, doi: [10.1111/j.1365-2966.2005.09560.x](https://doi.org/10.1111/j.1365-2966.2005.09560.x)
- Evirgen, C. C., Gent, F. A., Shukurov, A., Fletcher, A., & Bushby, P. 2017, *MNRAS*, 464, L105, doi: [10.1093/mnras/slw196](https://doi.org/10.1093/mnras/slw196)
- Federrath, C. 2016, *NewA*, 82, 535820601, doi: [10.1017/S0022377816001069](https://doi.org/10.1017/S0022377816001069)
- Ferrarese, L., Mould, J. R., Stetson, P. B., et al. 2007, *ApJ*, 654, 186, doi: [10.1086/506612](https://doi.org/10.1086/506612)
- Fletcher, A., Beck, R., Shukurov, A., Berkhuijsen, E. M., & Horellou, C. 2011, *MNRAS*, 412, 2396, doi: [10.1111/j.1365-2966.2010.18065.x](https://doi.org/10.1111/j.1365-2966.2010.18065.x)
- Font, J., Beckman, J. E., James, P. A., & Patsis, P. A. 2019, *MNRAS*, 482, 5362, doi: [10.1093/mnras/sty2983](https://doi.org/10.1093/mnras/sty2983)
- Frick, P., Stepanov, R., Beck, R., et al. 2016a, *A&A*, 585, A21, doi: [10.1051/0004-6361/201526796](https://doi.org/10.1051/0004-6361/201526796)
- . 2016b, *A&A*, 585, A21, doi: [10.1051/0004-6361/201526796](https://doi.org/10.1051/0004-6361/201526796)
- Gent, F. A. 2012, PhD thesis, Newcastle University
- Gressel, O., Elstner, D., Ziegler, U., & Rüdiger, G. 2008a, *A&A*, 486, L35, doi: [10.1051/0004-6361:200810195](https://doi.org/10.1051/0004-6361:200810195)
- Gressel, O., Ziegler, U., Elstner, D., & Rüdiger, G. 2008b, *Frontiers in Astronomy and Space Sciences*, 329, 619, doi: [10.1002/asna.200811005](https://doi.org/10.1002/asna.200811005)
- Harper, D. A., Runyan, M. C., Dowell, C. D., et al. 2018, *Journal of Astronomical Instrumentation*, 7, 1840008, doi: [10.1142/S2251171718400081](https://doi.org/10.1142/S2251171718400081)
- Haverkorn, M., Brown, J. C., Gaensler, B. M., & McClure-Griffiths, N. M. 2008a, *ApJ*, 680, 362, doi: [10.1086/587165](https://doi.org/10.1086/587165)
- . 2008b, *ApJ*, 680, 362, doi: [10.1086/587165](https://doi.org/10.1086/587165)
- Heald, G., Braun, R., & Edmonds, R. 2009, *A&A*, 503, 409, doi: [10.1051/0004-6361/200912240](https://doi.org/10.1051/0004-6361/200912240)
- Heesen, V., Beck, R., Krause, M., & Dettmar, R. J. 2011, *A&A*, 535, A79, doi: [10.1051/0004-6361/201117618](https://doi.org/10.1051/0004-6361/201117618)
- Hsieh, P.-Y., Matsushita, S., Liu, G., et al. 2011, *ApJ*, 736, 129, doi: [10.1088/0004-637X/736/2/129](https://doi.org/10.1088/0004-637X/736/2/129)
- Hummel, E., Lesch, H., Wielebinski, R., & Schlickeiser, R. 1988, *A&A*, 197, L29
- Hunter, J. D. 2007, *Computing in Science & Engineering*, 9, 3
- Izumi, T., Wada, K., Fukushige, R., Hamamura, S., & Kohno, K. 2018, *ApJ*, 867, 48, doi: [10.3847/1538-4357/aae20b](https://doi.org/10.3847/1538-4357/aae20b)
- Jones, K. L., Koribalski, B. S., Elmouttie, M., & Haynes, R. F. 1999, *MNRAS*, 302, 649, doi: [10.1046/j.1365-8711.1999.02057.x](https://doi.org/10.1046/j.1365-8711.1999.02057.x)
- Jones, T. J., Dowell, C. D., Lopez Rodriguez, E., et al. 2019, *ApJL*, 870, L9, doi: [10.3847/2041-8213/aaf8b9](https://doi.org/10.3847/2041-8213/aaf8b9)
- Karachentsev, I. D., Sharina, M. E., & Huchtmeier, W. K. 2000, *A&A*, 362, 544. <https://arxiv.org/abs/astro-ph/0010148>
- Kennicutt, Robert C., J., Armus, L., Bendo, G., et al. 2003, *PASP*, 115, 928, doi: [10.1086/376941](https://doi.org/10.1086/376941)
- Kim, W.-T., & Stone, J. M. 2012, *ApJ*, 751, 124, doi: [10.1088/0004-637X/751/2/124](https://doi.org/10.1088/0004-637X/751/2/124)
- Krause, M., Irwin, J., Schmidt, P., et al. 2020, *A&A*, 639, A112, doi: [10.1051/0004-6361/202037780](https://doi.org/10.1051/0004-6361/202037780)
- Kulsrud, R. M., & Zweibel, E. G. 2008, *Reports on Progress in Physics*, 71, 046901, doi: [10.1088/0034-4885/71/4/046901](https://doi.org/10.1088/0034-4885/71/4/046901)
- Kuno, N., Sato, N., Nakanishi, H., et al. 2007, *PASJ*, 59, 117, doi: [10.1093/pasj/59.1.117](https://doi.org/10.1093/pasj/59.1.117)
- Lin, C. C., & Shu, F. H. 1964, *ApJ*, 140, 646, doi: [10.1086/147955](https://doi.org/10.1086/147955)
- Lopez-Rodriguez, E. 2021a, *Nature Astronomy*, doi: [10.1038/s41550-021-01329-9](https://doi.org/10.1038/s41550-021-01329-9)
- . 2021b, *Nature Astronomy*, 5, 604, doi: [10.1038/s41550-021-01329-9](https://doi.org/10.1038/s41550-021-01329-9)
- Lopez-Rodriguez, E., Guerra, J. A., Asgari-Targhi, M., & Schmelz, J. T. 2021a, *ApJ*, 914, 24, doi: [10.3847/1538-4357/abf934](https://doi.org/10.3847/1538-4357/abf934)
- . 2021b, *ApJ*, 914, 24, doi: [10.3847/1538-4357/abf934](https://doi.org/10.3847/1538-4357/abf934)
- Lopez-Rodriguez, E., Dowell, C. D., Jones, T. J., et al. 2020a, *ApJ*, 888, 66, doi: [10.3847/1538-4357/ab5849](https://doi.org/10.3847/1538-4357/ab5849)
- . 2020b, *ApJ*, 888, 66, doi: [10.3847/1538-4357/ab5849](https://doi.org/10.3847/1538-4357/ab5849)
- Lopez-Rodriguez, E., Beck, R., Clark, S. E., et al. 2021c, *ApJ*, 923, 150, doi: [10.3847/1538-4357/ac2e01](https://doi.org/10.3847/1538-4357/ac2e01)
- Lopez-Rodriguez, E., Mao, S. A., Beck, R., et al. 2022a, *ApJ*, 936, 92, doi: [10.3847/1538-4357/ac7f9d](https://doi.org/10.3847/1538-4357/ac7f9d)
- Lopez-Rodriguez, E., Borlaff, A. S., Beck, R., et al. 2022b, *arXiv e-prints*, arXiv:2211.00012. <https://arxiv.org/abs/2211.00012>

- Lopez-Rodriguez, E., Clarke, M., Shenoy, S., et al. 2022c, *ApJ*, 936, 65, doi: [10.3847/1538-4357/ac83ac](https://doi.org/10.3847/1538-4357/ac83ac)
- Lou, Y.-Q., & Fan, Z. 1998, *ApJ*, 493, 102, doi: [10.1086/305114](https://doi.org/10.1086/305114)
- Lucero, D. M., Carignan, C., Elson, E. C., et al. 2015, *MNRAS*, 450, 3935, doi: [10.1093/mnras/stv856](https://doi.org/10.1093/mnras/stv856)
- Maiolino, R., Alonso-Herrero, A., Anders, S., et al. 2000, *ApJ*, 531, 219, doi: [10.1086/308444](https://doi.org/10.1086/308444)
- Martin-Alvarez, S., Devriendt, J., Slyz, A., et al. 2022, *MNRAS*, 513, 3326, doi: [10.1093/mnras/stac1099](https://doi.org/10.1093/mnras/stac1099)
- Martin-Alvarez, S., Slyz, A., Devriendt, J., & Gómez-Guijarro, C. 2020, *MNRAS*, 495, 4475, doi: [10.1093/mnras/staa1438](https://doi.org/10.1093/mnras/staa1438)
- Martini, P., Regan, M. W., Mulchaey, J. S., & Pogge, R. W. 2003, *ApJS*, 146, 353, doi: [10.1086/367817](https://doi.org/10.1086/367817)
- Mayya, Y. D., Carrasco, L., & Luna, A. 2005, *ApJL*, 628, L33, doi: [10.1086/432644](https://doi.org/10.1086/432644)
- McQuinn, K. B. W., Skillman, E. D., Dolphin, A. E., Berg, D., & Kennicutt, R. 2017, *AJ*, 154, 51, doi: [10.3847/1538-3881/aa7aad](https://doi.org/10.3847/1538-3881/aa7aad)
- Mestel, L., & Subramanian, K. 1991, *MNRAS*, 248, 677, doi: [10.1093/mnras/248.4.677](https://doi.org/10.1093/mnras/248.4.677)
- Mouschovias, T. C., & Ciolek, G. E. 1999, in *NATO Advanced Study Institute (ASI) Series C, Vol. 540, The Origin of Stars and Planetary Systems*, ed. C. J. Lada & N. D. Kylafis, 305
- Ntormousi, E., Tassis, K., Del Sordo, F., Fragkoudi, F., & Pakmor, R. 2020, *A&A*, 641, A165, doi: [10.1051/0004-6361/202037835](https://doi.org/10.1051/0004-6361/202037835)
- Patrikeev, I., Fletcher, A., Stepanov, R., et al. 2006, *A&A*, 458, 441, doi: [10.1051/0004-6361:20065225](https://doi.org/10.1051/0004-6361:20065225)
- Pattle, K., Fissel, L., Tahani, M., Liu, T., & Ntormousi, E. 2022, *arXiv e-prints*, arXiv:2203.11179, <https://arxiv.org/abs/2203.11179>
- Pillai, T. G. S., Clemens, D. P., Reissl, S., et al. 2020, *Nature Astronomy*, 4, 1195, doi: [10.1038/s41550-020-1172-6](https://doi.org/10.1038/s41550-020-1172-6)
- Quillen, A. C., Neumayer, N., Oosterloo, T., & Espada, D. 2010, *PASA*, 27, 396, doi: [10.1071/AS09069](https://doi.org/10.1071/AS09069)
- Radburn-Smith, D. J., de Jong, R. S., Seth, A. C., et al. 2011, *ApJS*, 195, 18, doi: [10.1088/0067-0049/195/2/18](https://doi.org/10.1088/0067-0049/195/2/18)
- Rees, M. J. 1987, *QJRAS*, 28, 197
- Rincon, F. 2019, *NewA*, 85, 205850401, doi: [10.1017/S0022377819000539](https://doi.org/10.1017/S0022377819000539)
- Robitaille, T., & Bressert, E. 2012, *APLpy: Astronomical Plotting Library in Python*. <http://ascl.net/1208.017>
- Roussel, H., Wilson, C. D., Vigroux, L., et al. 2010, *A&A*, 518, L66, doi: [10.1051/0004-6361/201014567](https://doi.org/10.1051/0004-6361/201014567)
- Ruiz-Granados, B., Rubiño-Martín, J. A., Florido, E., & Battaner, E. 2010, *ApJ*, 723, L44, doi: [10.1088/2041-8205/723/1/L44](https://doi.org/10.1088/2041-8205/723/1/L44)
- Ruzmaikin, A., Sokolov, D., & Shukurov, A. 1988, *Nature*, 336, 341, doi: [10.1038/336341a0](https://doi.org/10.1038/336341a0)
- Sellwood, J. A. 2011, *MNRAS*, 410, 1637, doi: [10.1111/j.1365-2966.2010.17545.x](https://doi.org/10.1111/j.1365-2966.2010.17545.x)
- Serkowski, K. 1974, *Methods of Experimental Physics*, 12, 361, doi: [10.1016/S0076-695X\(08\)60500-1](https://doi.org/10.1016/S0076-695X(08)60500-1)
- Seta, A., & Federrath, C. 2022, *MNRAS*, 514, 957, doi: [10.1093/mnras/stac1400](https://doi.org/10.1093/mnras/stac1400)
- Shukurov, A. 1998, *MNRAS*, 299, L21, doi: [10.1046/j.1365-8711.1998.01958.x](https://doi.org/10.1046/j.1365-8711.1998.01958.x)
- Soida, M., Urbanik, M., Beck, R., Wielebinski, R., & Balkowski, C. 2001, *A&A*, 378, 40, doi: [10.1051/0004-6361:20011185](https://doi.org/10.1051/0004-6361:20011185)
- Sokoloff, D. D., Bykov, A. A., Shukurov, A., et al. 1998, *MNRAS*, 299, 189, doi: [10.1046/j.1365-8711.1998.01782.x](https://doi.org/10.1046/j.1365-8711.1998.01782.x)
- Subramanian, K. 2016, *Reports on Progress in Physics*, 79, 076901, doi: [10.1088/0034-4885/79/7/076901](https://doi.org/10.1088/0034-4885/79/7/076901)
- Surgent, W. J., Lopez-Rodriguez, E., & Clark, S. E. 2023, *arXiv e-prints*, arXiv:2302.07278, doi: [10.48550/arXiv.2302.07278](https://doi.org/10.48550/arXiv.2302.07278)
- Tahani, M., Glover, J., Lupypciw, W., et al. 2022a, *A&A*, 660, L7, doi: [10.1051/0004-6361/202243322](https://doi.org/10.1051/0004-6361/202243322)
- Tahani, M., Lupypciw, W., Glover, J., et al. 2022b, *A&A*, 660, A97, doi: [10.1051/0004-6361/202141170](https://doi.org/10.1051/0004-6361/202141170)
- Tarchi, A., Greve, A., Peck, A. B., et al. 2004, *MNRAS*, 351, 339, doi: [10.1111/j.1365-2966.2004.07792.x](https://doi.org/10.1111/j.1365-2966.2004.07792.x)
- Tully, R. B. 1988, *Nearby galaxies catalog*
- Tully, R. B., Rizzi, L., Shaya, E. J., et al. 2009, *AJ*, 138, 323, doi: [10.1088/0004-6256/138/2/323](https://doi.org/10.1088/0004-6256/138/2/323)
- Tully, R. B., Courtois, H. M., Dolphin, A. E., et al. 2013, *AJ*, 146, 86, doi: [10.1088/0004-6256/146/4/86](https://doi.org/10.1088/0004-6256/146/4/86)
- Vacca, W. D., Hamilton, R. T., Savage, M., et al. 2015, *ApJ*, 804, 66, doi: [10.1088/0004-637X/804/1/66](https://doi.org/10.1088/0004-637X/804/1/66)
- Vaillancourt, J. E., Chuss, D. T., Crutcher, R. M., et al. 2007, in *Society of Photo-Optical Instrumentation Engineers (SPIE) Conference Series*, Vol. 6678, *Proc. SPIE*, 66780D, doi: [10.1117/12.730922](https://doi.org/10.1117/12.730922)
- van de Voort, F., Bieri, R., Pakmor, R., et al. 2021, *MNRAS*, 501, 4888, doi: [10.1093/mnras/staa3938](https://doi.org/10.1093/mnras/staa3938)
- Verstappen, J., Fritz, J., Baes, M., et al. 2013, *A&A*, 556, A54, doi: [10.1051/0004-6361/201220733](https://doi.org/10.1051/0004-6361/201220733)
- Widrow, L. M. 2002, *Rev. Mod. Phys.*, 74, 775, doi: [10.1103/RevModPhys.74.775](https://doi.org/10.1103/RevModPhys.74.775)
- Wiegert, T., Irwin, J., Miskolczi, A., et al. 2015, *AJ*, 150, 81, doi: [10.1088/0004-6256/150/3/81](https://doi.org/10.1088/0004-6256/150/3/81)
- Willick, J. A., Courteau, S., Faber, S. M., et al. 1997, *ApJS*, 109, 333, doi: [10.1086/312983](https://doi.org/10.1086/312983)
- Zschaechner, L. K., Walter, F., Bolatto, A., et al. 2016, *ApJ*, 832, 142, doi: [10.3847/0004-637X/832/2/142](https://doi.org/10.3847/0004-637X/832/2/142)